

Mechanics of Advanced Materials and Structures

ISSN: (Print) (Online) Journal homepage: https://www.tandfonline.com/loi/umcm20

Thermo-elastic buckling behaviors of advanced fluid-infiltrated porous shells integrated with GPLs-reinforced nanocomposite patches

Ehsan Arshid, Mohammad Amin Ghorbani, Mohammad Javad Momeni Nia, Ömer Civalek & Abhinav Kumar

To cite this article: Ehsan Arshid, Mohammad Amin Ghorbani, Mohammad Javad Momeni Nia, Ömer Civalek & Abhinav Kumar (2023): Thermo-elastic buckling behaviors of advanced fluid-infiltrated porous shells integrated with GPLs-reinforced nanocomposite patches, Mechanics of Advanced Materials and Structures, DOI: 10.1080/15376494.2023.2251015

To link to this article: https://doi.org/10.1080/15376494.2023.2251015

Published online: 28 Aug 2023.

Submit your article to this journal

View related articles

View Crossmark data

Full Terms & Conditions of access and use can be found at
https://www.tandfonline.com/action/journalInformation?journalCode=umcm20

MECHANICS OF ADVANCED MATERIALS AND STRUCTURES
https://doi.org/10.1080/15376494.2023.2251015

Taylor & Francis
Taylor & Francis Group

ORIGINAL ARTICLE

Check for updates

Thermo-elastic buckling behaviors of advanced fluid-infiltrated porous shells integrated with GPLs-reinforced nanocomposite patches

Ehsan Arshid[a], Mohammad Amin Ghorbani[b], Mohammad Javad Momeni Nia[b], Ömer Civalek[c], and Abhinav Kumar[d]

[a]Advanced Research and Development Center, LIPS Research Foundation, European International University, Paris, France; [b]Department of Mechanical Engineering, Qom Branch, Islamic Azad University, Qom, Iran; [c]China Medical University, Taichung, Taiwan; [d]Department of Nuclear and Renewable Energy, Ural Federal University Named After the First President of Russia, Ekaterinburg, Russia

ABSTRACT

In the existing paper, thermo-mechanical buckling performance of three-layered advanced fluid-infiltrated porous shells that are embedded between two GPLs-reinforced composite layers is investigated. The influence of the fluids in the pores is investigated using Skempton coefficient. Imperfection types and ratio effects are also considered. Moreover, for the face layers, Graphene nanoplatelets (GPLs) weight fraction and dispersion patterns are studied. After deriving the governing equations employing virtual displacement method, they are solved analytically *via* Navier's approach. Finally, the impact of different factors on the critical buckling loads (CBLs) and temperatures (CBTs) of cylindrical, spherical, and doubly-curved shells is assessed.

ARTICLE HISTORY
Received 18 July 2023
Accepted 18 August 2023

KEYWORDS
Graphene nanoplatelets; fluid-infiltrated porous materials; thermo-elastic buckling; first-order shear deformation theory; doubly-curved shell; sandwich structures

1. Introduction

Due to the need to improve the performance of engineering structures by academics, therefore, they are motivated to consider different shapes of them and also, different materials to realize their response against different loading and environmental conditions [1, 2]. Functionally graded (FG) materials are used nowadays instead of former homogenous ones to advance the mechanical behaviors of structures. In FG materials, the mechanical properties of the structure change incessantly in a specific course such as thickness or length [3]. Porous materials also are used widely due to their lightweight and strength together [4, 5]. But, as the porosity increases, their stiffness reduces. Detournay and Cheng [6] proposed the fundamental equations for porous materials in two cases: saturated and unsaturated conditions. Their work was formed on the basis of Biot's poroelasticity theory. Porosity or the same imperfection ratio designates the pores to bulk volume ratio and its' enhancement shows the porous structures' weaknesses. To overcome this deficiency, they should be reinforced somehow [7]. One of the most well-known ways is to attach two layers from a stiffer material to its surfaces. The structure with a softer mid-layer (which is recognized as core), and two stiffer layers on its surfaces is called sandwich structures. The martial type of the faces is a key factor in the mechanical performance of the structure. As their stiffness-to-weight ratio becomes higher, they are better choice for use in structures [8]. This aim can be touched using nanocomposites. Nanocomposites are called a kind of composite that as a minimum one of its components is in nanoscale [9]. The most popular nanocomposites are those that are reinforced by carbon nanotubes (CNTs) and graphene nanoplatelets (GPLs). These two kinds of nanofillers have extreme thermomechanical specifications such as sound and energy absorption, high stiffness, high thermal capacity, and so on [10–12]. CNTs and GPLs' effect on the mechanical manners of structures considered by earlier works that showed GPLs are even can be a better selection. For instance, Sobhani et al. [13, 14] compared the influence of two types of nanofillers, namely GPLs and CNTs to determine the most appropriate condition for the vibrational performance of shells. They concluded that GPLs make the structure stiffer. Numerous works by different researchers are provided to consider the static and dynamic performance of shells. In the following, some of their most relevant to the current work will be reviewed. Trinh and Kim [15] took an FG doubly-curved into investigation and considered its static and dynamic behaviors. They used a three-variable theory to describe the displacements. Finally, they resulted the porosity distribution types have a noteworthy effect on the results. Vibrations of a doubly-curved piezoelectric shell regarding the geometrical nonlinearity provided by Zhu et al. [16]. They utilized the harmonic balance scheme to derive the frequencies. Also, Zhao et al. [17] obtained frequencies of an FG porous doubly-curved shell considering classical boundary conditions with the assistance

CONTACT Ehsan Arshid ehsanarshid@gmail.com Advanced Research and Development Center, LIPS Research Foundation, European International University, Paris, France; Ömer Civalek civalek@yahoo.com China Medical University, Taichung, Taiwan.

© 2023 Taylor & Francis Group, LLC

of a semi-analytical scheme. Wang et al. [18] investigated vibration and bending behaviors of FG nanocomposite doubly-curved shallow shells reinforced by GPLs. Nonlinear vibrations of GPL-reinforced piezoelectric composite plate under external voltage excitation considered by Mao and Zhang [19]. They also provided another research [20] on buckling and post-buckling analyses of FG GPL-reinforced piezoelectric plate subjected to electric potential and axial forces. Wang and Zhang [21] studied the thermal buckling and post-buckling responses of temperature-dependent GPL-reinforced porous nanocomposite beams. They concluded that effects of internal pores and GPLs on thermal stabilities of beams were strongly dependent on distribution patterns. Talebitooti and Zarastvand [22] studied the influence of porous materials' nature on the mechanical behavior of doubly-curved sandwich shells. Aminipour et al. [23] conducted a study on doubly-curved nanoshells made of various materials with FG properties. They considered the shear deformation influence using a higher-order theory. Sayyad and Ghugal [24] conducted a study where they used different shell theories that were equivalent in order to examine the effects of shear deformation and rotary inertia on both static and dynamic analyses of doubly-curved shells made of FG materials. A novel modified quasi-3D theory was used by Rachid et al. [25] to examine mechanical behavior of FG doubly-curved panels. Karami et al. [26] conducted their study on the temperature and porosity-dependent dynamic behavior of doubly-curved nanoshells. They used a nonlocal strain gradient theory to reach this aim. An imperfect shallow doubly-curved nanoshell took into examined by Ahmadi et al. [27] which was located on elastic substrate and in thermal environment. Xue et al. [28] demonstrated the use of isogeometric analysis to solve the problem of free vibrations in functionally graded porous cylindrical panels. They employed the FSDT approach and examined the impact of the imperfection ratio on the natural frequencies. Cong and Duc [29] considered a porous eccentrically stiffened doubly-curved shell with negative Poisson's ratio. The shell was exposed to blast, mechanical, and thermal loads. The frequencies of a porous doubly-curved panel with CNT-reinforced patches were obtained by Setoodeh et al. [30]. They formulated equations using a generalized shear deformation theory and obtained the results with the assistance of generalized differential quadrature method. Their findings indicated that the vibrational characteristics of the structure are significantly affected by the volume fraction of carbon nanotubes. Karimiasl et al. [31] considered nonlinear vibrations of a doubly-curved shell with different layer arrangements including CNTs. They utilized the multiple scale method to report their findings. A quasi-3D theory was hired by Duong et al. [32] to consider the boundary influence on static response of CNT-reinforced cylindrical shells. Yang et al. [33] conducted an investigation of a cylindrical panel strengthened with GPL and determined its natural frequencies and critical buckling loads (CBLs). They used the FSDT in their analysis. Ma et al. [34] established a finite element model to explore the buckling behavior of cylindrical shells. Their study focused on the sensitivity of cylindrical shells to imperfections exposed to localized axial compression loads in multiple regions. Gui and Mu [35] calculated the CBLs of cylindrical shells in 2023. They captured the scale effect *via* the nonlocal strain gradient theory. Buckling and post-buckling performances of FG doubly-curved shells were discussed by Quan et al. [36]. They examined two types of sandwich structures. Besides, other studies were conducted by frequent researchers to study mechanical response of curved shells as can be seen in Refs. [37–51].

Revising the study background demonstrates the absence of research on thermo-elastic buckling of different categories of three-layered advanced curved shells including cylindrical, spherical, and doubly-curved types. The curved structure core is made from lightweight porous fluid-infiltrated materials that are bounded by two stiffer nanocomposite skins. In this recent work, the pressure of the pores is being examined for its influence on this particular structure, marking the first time it has been studied. Also, different imperfection types which show the pores' placement are explored. The nanocomposite faces are reinforced by GPLs to advance their thermomechanical properties. Furthermore, it is presumed that GPLs are dispersed across the faces' thickness considering different specified FG patterns. The curved shells are immersed in a set of springs and shear layer which is named Pasternak substrate. The equations were attained by means of the virtual displacement principle, then analytically solved, and finally, they will be authenticated with the reliable former published works. Next, the study thoroughly examines and discusses the impact of the key factors on the results. The findings of this research, given the aforementioned specifications of the model, can be applied to various scientific disciplines, including energy absorption, thermal management, aerospace, high-speed trains, air travel, and other engineering structures and industries.

2. Model description

As detailed in the past section and as exemplified in Figure 1, the used model consists of a three-layered doubly-curved shell with GPL-reinforced composite skins and a porous core infiltrated with fluid. The shell is situated on a Pasternak substrate. Also, this figure displays the geometric

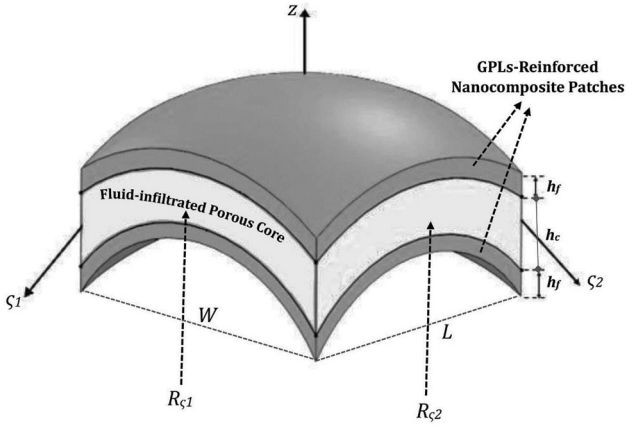


Figure 1. Schematic diagram of the under consideration saturated porous sandwich curved structures.

measurements of the shell. To initiate modeling of the aforesaid structure, primarily, the constitutive relations of the three layers will be depicted. The constitutive law for all three layers in thermal environment can be established as [52, 53]:

$$\sigma_{ij}^{c,f} = Q_{ijkl}^{c,f}(z)\varepsilon_{kl} - \alpha_{c,f}(z)\Delta T\delta_{ij}, \tag{1}$$

In which stress and strain components are shown by σ_{ij} and ε_{kl}, respectively. The thermal expansion coefficient is presented by $\alpha(z)$, and the temperature differences is publicized by ΔT. Stiffness matrix components (Q_{ijkl}) are defined separately for each layer. For the nanocomposite faces, they are defined as below [54]:

$$Q_{11}^{f}(z) = Q_{22}^{f}(z) = \frac{E_f(z)}{1-\nu_f(z)^2}, \quad Q_{12}^{f}(z) = Q_{21}^{f}(z) = \nu_f(z)Q_{11}^{f}(z),$$
$$Q_{44}^{f}(z) = Q_{55}^{f}(z) = Q_{66}^{f}(z) = \frac{E_f(z)}{2(1+\nu_f(z))} \tag{2}$$

where the subscript "*f*" signifies the faces. There are different ways to estimate the thermo-mechanical properties of GPL-reinforced nanocomposites, but two common methods are Halpin-Tsai and the rule of mixture. Halpin-Tsai is hired to forecast Young's modulus, while the rule of mixture is employed to predict other properties by assuming the composite behaves like a mixture of its individual components. So, the properties of the face sheets, with exception of Young's modulus can be yielded as [55]:

$$\rho_f(z) = \rho_{GPL}V_{GPL} + \rho_m V_m, \tag{3}$$

$$\alpha_f(z) = (V_{GPL}E_{GPL}\alpha_{GPL} + V_m E_m \alpha_m)/(V_{GPL}E_{GPL} + V_m E_m), \tag{4}$$

$$\nu_f(z) = \nu_{GPL}V_{GPL} + \nu_m V_m \tag{5}$$

It is noteworthy that V_{GPL} and V_m are volume fraction of GPLs and the matrix, correspondingly whose summations equal one and E_m denotes to matrix Young's elasticity modulus. Also, the Halpin-Tsai scheme can aids to obtain the actual Young's modulus as [56]:

$$E_f(z) = \frac{\left(3\left(\frac{1+\xi_l^{GPL}\chi_l^{GPL}V_{GPL}}{1-\chi_l^{GPL}V_{GPL}}\right) + 5\left(\frac{1+\xi_w^{GPL}\chi_w^{GPL}V_{GPL}}{1-\chi_w^{GPL}V_{GPL}}\right)\right)}{8}E_m \tag{6}$$

GPLs' geometry parameters are publicized by ξ_l^{GPL} and ξ_w^{GPL} [57]:

$$\xi_l^{GPL} = \frac{2l_{GPL}}{h_{GPL}}, \quad \xi_w^{GPL} = \frac{2w_{GPL}}{h_{GPL}} \tag{7}$$

in these relations, the length, height, and width of the GPLs are offered by l_{GPL}, h_{GPL}, and w_{GPL}, one-to-one. Also, material parameters are shown in Eq. (6) by χ_l^{GPL} and χ_w^{GPL} which are defined as [58]:

$$\chi_l^{GPL} = \frac{h_{GPL}(E_R-1)}{h_{GPL}E_R + 2l_{GPL}}, \quad \chi_w^{GPL} = \frac{h_{GPL}(E_R-1)}{h_{GPL}E_R + 2w_{GPL}} \tag{8}$$

where E_R denotes the ratio of Young's modulus of GPLs to the matrix.

GPLs are dispersed across the faces' thickness (h_f) based on five distinguished FG patterns:

$$V_{GPL}(z) = V_{GPL}^{*} \quad \text{Uniform Pattern} \tag{9}$$

$$V_{GPL}(z) = \left(1 - \frac{2z}{h_f}\right)V_{GPL}^{*} \quad \text{FG} - \text{A Pattern} \tag{10}$$

$$V_{GPL}(z) = \left(1 + \frac{2z}{h_f}\right)V_{GPL}^{*} \quad \text{FG} - \text{V Pattern} \tag{11}$$

$$V_{GPL}(z) = 2\left(1 - \frac{2z}{h_f}\right)V_{GPL}^{*} \quad \text{FG} - \text{O Pattern} \tag{12}$$

$$V_{GPL}(z) = \frac{4|z|}{h_f}V_{GPL}^{*} \quad \text{FG} - \text{X Pattern} \tag{13}$$

Furthermore, the stiffness components for the fluid-infiltrated porous core can be stated in terms of the drained (ν) and undrained (ν_u) Poisson's ratio as [59]:

$$Q_{11}^{c}(z) = Q_{22}^{c}(z) = 2G_c(z)\frac{1-4\nu+2\nu_u}{1-3\nu+2\nu\nu_u}, \tag{14}$$

$$Q_{12}^{c}(z) = Q_{21}^{c}(z) = 2G_c(z)\frac{-\nu+2(1-\nu)\nu_u}{1-3\nu+2\nu\nu_u} \tag{15}$$

where [60]:

$$\nu_u = (3\nu+\Delta)/(3-\Delta) \tag{16}$$

in which Δ=$B\lambda(z)(1\text{-}2\nu)$; where the Skempton coefficient is depicted by B that demonstrates the pressure of the fluid inside the pores, $\lambda(z)$ is the Biot's coefficient, that can be determined *via* $1\text{-}G_c(z)/G_0$. Also, $G_c(z)$ equals $E_c(z)/2(1+\nu_c)$. $E_c(z)$ is Young's elasticity modulus of the core. The core's thermo-mechanical properties can be adjusted based on its thickness using the equations provided below [61]:

$$\begin{Bmatrix} E_c(z) \\ \rho_c(z) \\ \alpha_c(z) \end{Bmatrix} = \begin{Bmatrix} E_1 \\ \rho_1 \\ \alpha_1 \end{Bmatrix}\left(1 - \begin{Bmatrix} \beta \\ 1-\sqrt{1-\beta} \\ 1-\sqrt{1-\beta} \end{Bmatrix}p(z)\right), \tag{17}$$

here, β is the imperfection ratio which is demarcated as the ratio of pores to the whole volume. Also, "*c*" subscript denotes the core, and "1" subscript denotes the maximum values of core's properties. $p(z)$ is the imperfection function which can be determined based on the following descriptions. Three distinguished types of imperfection or the same pores' distribution are considered in the current study:

– Imperfection Type A:

The primary examined type is entitled "Type A" in the recent paper, in which the pores are scattered non-symmetrically concerning the core's mid-plane. Therefore, for this pattern, the function $p(z)$ is introduced as [62]:

$$p(z) = \cos\left[\frac{\pi}{2h_c}\left(z + \frac{h_c}{2}\right)\right], \tag{18}$$

– Imperfection Type B:

The second explored porosity pattern that is known as "Type B" in this paper which follows the below function [63]:

$$p(z) = \cos\left(\frac{\pi z}{h_c}\right), \tag{19}$$

– Imperfection Type C:
The third considered pattern is a "Type C" one that thickness-free. For this pattern, the below relations for Young's modulus and density are ruled [64]:

$$E_c(z) = E_1(1-\beta\chi), \rho_c(z) = \rho_1\sqrt{1-\beta\chi}, \alpha_c(z) = \alpha_1\sqrt{1-\beta\chi} \tag{20}$$

where

$$\chi = \frac{1}{\beta} - \frac{1}{\beta}\left(\frac{2}{\pi}\sqrt{1-\beta} - \frac{2}{\pi} + 1\right)^2 \tag{21}$$

3. Governing equations derivation procedure

In this study, the shear deformation effect is accounted for to achieve more precise outcomes. To this aim, the FSDT suggests the displacements as [65]:

$$u_{\varsigma_1}(\varsigma_1, \varsigma_2, z) = \mu_{\varsigma_1} u(\varsigma_1, \varsigma_2) + z\psi_{\varsigma_1}(\varsigma_1, \varsigma_2), \tag{22}$$

$$u_{\varsigma_2}(\varsigma_1, \varsigma_2, z) = \mu_{\varsigma_2} v(\varsigma_1, \varsigma_2) + z\psi_{\varsigma_2}(\varsigma_1, \varsigma_2),$$

$$u_z(\varsigma_1, \varsigma_2, z) = w(\varsigma_1, \varsigma_2)$$

The displacement of any point on the shell in the ς_1, ς_2 and z paths is characterized by $u_{\varsigma 1}$, $u_{\varsigma 2}$ and u_z, correspondingly. The mid-plane displacement components in the same courses are denoted by u, v and w. Additionally, $\psi_{\varsigma 1}$ and $\psi_{\varsigma 2}$ link to the rotation of the mid-plane about the x_2 and x_1 axes, one-to-one and:

$$\mu_{\varsigma_1} = 1 + \frac{z}{R_{\varsigma_1}}, \quad \mu_{\varsigma_2} = 1 + \frac{z}{R_{\varsigma_2}} \tag{23}$$

The strains can be expressed using the displacements based on the FSDT as [66]:

$$\varepsilon_{\varsigma_1\varsigma_1} = \frac{\partial u}{\partial \varsigma_1} + \frac{w}{R_{\varsigma_1}} + z\frac{\partial \psi_{\varsigma_1}}{\partial \varsigma_1}, \tag{24}$$

$$\varepsilon_{\varsigma_2\varsigma_2} = \frac{\partial v}{\partial \varsigma_2} + \frac{w}{R_{\varsigma_2}} + z\frac{\partial \psi_{\varsigma_2}}{\partial \varsigma_2}, \tag{25}$$

$$\gamma_{\varsigma_1\varsigma_2} = \frac{\partial u}{\partial \varsigma_2} + \frac{\partial v}{\partial \varsigma_1} + z\left(\frac{\partial \psi_{\varsigma_1}}{\partial \varsigma_2} + \frac{\partial \psi_{\varsigma_2}}{\partial \varsigma_1} - \left(\frac{R_{\varsigma_2} - R_{\varsigma_1}}{2R_{\varsigma_1}R_{\varsigma_2}}\right)\left(\frac{\partial v}{\partial \varsigma_1} - \frac{\partial u}{\partial \varsigma_2}\right)\right), \tag{26}$$

$$\gamma_{\varsigma_1 z} = \psi_{\varsigma_1} + \frac{\partial w}{\partial \varsigma_1} - \frac{u}{R_{\varsigma_1}}, \tag{27}$$

$$\gamma_{\varsigma_2 z} = \psi_{\varsigma_2} + \frac{\partial w}{\partial \varsigma_2} - \frac{v}{R_{\varsigma_2}} \tag{28}$$

With the aim of obtaining the equations, firstly the strain energy should be obtained. To reach this goal, the below equation can be used [67]:

$$U = \frac{1}{2}\int_{-h/2}^{h/2}\int_{\varsigma_1}\int_{\varsigma_2}(\sigma_{\varsigma_1\varsigma_1}\varepsilon_{\varsigma_1\varsigma_1} + \sigma_{\varsigma_2\varsigma_2}\varepsilon_{\varsigma_2\varsigma_2} + \tau_{\varsigma_1\varsigma_2}\gamma_{\varsigma_1\varsigma_2} + \tau_{\varsigma_1 z}\gamma_{\varsigma_1 z} + \tau_{\varsigma_2 z}\gamma_{\varsigma_2 z})\,\mathrm{d}A\mathrm{d}z \tag{29}$$

Which its variations lead to the following equation:

$$\delta U = \int_{-h/2}^{h/2}\int_{\varsigma_1}\int_{\varsigma_2}(\sigma_{\varsigma_1\varsigma_1}\delta\varepsilon_{\varsigma_1\varsigma_1} + \sigma_{\varsigma_2\varsigma_2}\delta\varepsilon_{\varsigma_2\varsigma_2} + \tau_{\varsigma_1\varsigma_2}\delta\gamma_{\varsigma_1\varsigma_2} + \tau_{\varsigma_1 z}\delta\gamma_{\varsigma_1 z} + \tau_{\varsigma_2 z}\delta\gamma_{\varsigma_2 z})\,\mathrm{d}A\mathrm{d}z \tag{30}$$

The external work involves of three portions: Pasternak substrate (E_P); thermal load (E_T); and mechanical in-plane load (E_M). Thus:

$$E = E_P + E_T + E_M, \tag{31}$$

The work of Pasternak substrate can be expressed as below [68]:

$$E_P = \frac{1}{2}\int_A \left[-\left(K_W w(\varsigma_1, \varsigma_2) - K_P\nabla^2 w(\varsigma_1, \varsigma_2)\right)w(\varsigma_1, \varsigma_2)\right]\mathrm{d}A \tag{32}$$

In this equation, Laplacian operator is shown by ∇^2; Springs and shear layer parameters are shown by K_W and K_P, individually.

One possible way to calculate thermal load work is using the following equation [69, 70]:

$$E_T = \frac{1}{2}\int_{\varsigma_1}\int_{\varsigma_2}\left\{N_{\varsigma_1}^T\left(\frac{\partial w(\varsigma_1, \varsigma_2)}{\partial \varsigma_1}\right)^2 + N_{\varsigma_2}^T\left(\frac{\partial w(\varsigma_1, \varsigma_2)}{\partial \varsigma_2}\right)^2\right\}\mathrm{d}A \tag{33}$$

in which axial and circumferential thermal loads are represented by $N_{\varsigma_1}^T$ and $N_{\varsigma_2}^T$ that are as introduced as [71]:

$$N_{\varsigma_1}^T = \int_{core,faces}\left(Q_{11}^{c,f}(z) + Q_{12}^{c,f}(z)\right)\alpha_{c,f}(z)\Delta T\mathrm{d}z, \tag{34}$$

$$N_{\varsigma_2}^T = \int_{core,faces}\left(Q_{12}^{c,f}(z) + Q_{22}^{c,f}(z)\right)\alpha_{c,f}(z)\Delta T\mathrm{d}z \tag{35}$$

And to achieve the work of mechanical in-plane load, the subsequent equation can be hired:

$$E_M = \frac{1}{2}\int_{\varsigma_1}\int_{\varsigma_2}\left\{N_{\varsigma_1}^M\left(\frac{\partial w(\varsigma_1, \varsigma_2)}{\partial \varsigma_1}\right)^2 + N_{\varsigma_2}^M\left(\frac{\partial w(\varsigma_1, \varsigma_2)}{\partial \varsigma_2}\right)^2\right\}\mathrm{d}A \tag{36}$$

in which axial and circumferential mechanical in-plane loads are symbolized by $N_{\varsigma_1}^M$ and $N_{\varsigma_2}^M$.

The equations can be obtained by applying the virtual displacement principle, which involves introducing variations of the strain energy and external work into the

equations [72]:

$$\delta(U-E)=0 \tag{37}$$

By expressing the strains in terms of the displacements and defining the stress resultants, the equilibrium equations in terms of stress resultants can be obtained using variational calculus as follows:

$$\delta u:$$

$$\frac{\partial N_{\varsigma_1\varsigma_1}}{\partial \varsigma_1}+\frac{\partial N_{\varsigma_1\varsigma_2}}{\partial \varsigma_2}+\left(\frac{R_{\varsigma_2}-R_{\varsigma_1}}{2R_{\varsigma_1}R_{\varsigma_2}}\right)\frac{\partial M_{\varsigma_1\varsigma_2}}{\partial \varsigma_2}+\frac{Q_{\varsigma_1}}{R_{\varsigma_1}}=0, \tag{38}$$

$$\delta v:$$

$$\frac{\partial N_{\varsigma_2\varsigma_2}}{\partial \varsigma_2}+\frac{\partial N_{\varsigma_1\varsigma_2}}{\partial \varsigma_1}-\left(\frac{R_{\varsigma_2}-R_{\varsigma_1}}{2R_{\varsigma_1}R_{\varsigma_2}}\right)\frac{\partial M_{\varsigma_1\varsigma_2}}{\partial \varsigma_1}+\frac{Q_{\varsigma_2}}{R_{\varsigma_2}}=0, \tag{39}$$

$$\delta w:$$

$$\begin{aligned}\frac{N_{\varsigma_1\varsigma_1}}{R_{\varsigma_1}}+\frac{N_{\varsigma_2\varsigma_2}}{R_{\varsigma_2}}-\frac{\partial Q_{\varsigma_1}}{\partial \varsigma_1}-\frac{\partial Q_{\varsigma_2}}{\partial \varsigma_2}-K_W\ w+K_P\ \frac{\partial^2 w}{\partial {\varsigma_1}^2}\\ +K_P\ \frac{\partial^2 w}{\partial {\varsigma_2}^2}+N^T_{\varsigma_1}\frac{\partial^2 w}{\partial {\varsigma_1}^2}+N^T_{\varsigma_2}\frac{\partial^2 w}{\partial {\varsigma_2}^2}\\ +N^M_{\varsigma_1}\frac{\partial^2 w}{\partial {\varsigma_1}^2}+N^M_{\varsigma_2}\frac{\partial^2 w}{\partial {\varsigma_2}^2}=0,\end{aligned} \tag{40}$$

$$\delta\varphi_{x_1}:$$

$$\frac{\partial M_{\varsigma_1\varsigma_1}}{\partial \varsigma_1}+\frac{\partial M_{\varsigma_1\varsigma_2}}{\partial \varsigma_2}-Q_{\varsigma_1}=0, \tag{41}$$

$$\delta\varphi_{x_2}:$$

$$\frac{\partial M_{\varsigma_1\varsigma_2}}{\partial \varsigma_1}+\frac{\partial M_{\varsigma_2\varsigma_2}}{\partial \varsigma_2}-Q_{\varsigma_2}=0 \tag{42}$$

The below equation defines the stress resultants that were utilized in the above relations:

$$\begin{aligned}N_{\varsigma_1\varsigma_1}=\eta_1\ \frac{\partial u}{\partial \varsigma_1}+\eta_2\ \frac{\partial \psi_{\varsigma_1}}{\partial \varsigma_1}+\frac{\eta_1 w}{R_{\varsigma_1}}+\eta_4\ \frac{\partial v}{\partial \varsigma_2}+\eta_5\ \frac{\partial \psi_{\varsigma_2}}{\partial \varsigma_2}\\ +\frac{\eta_4 w}{R_{\varsigma_2}},\end{aligned} \tag{43}$$

$$\begin{aligned}N_{\varsigma_2\varsigma_2}=\eta_7\ \frac{\partial u}{\partial \varsigma_1}+\eta_8\ \frac{\partial \psi_{\varsigma_1}}{\partial \varsigma_1}+\frac{\eta_7 w}{R_{\varsigma_1}}+\eta_{10}\ \frac{\partial v}{\partial \varsigma_2}+\eta_{11}\ \frac{\partial \psi_{\varsigma_2}}{\partial \varsigma_2}\\ +\frac{\eta_{10} w}{R_{\varsigma_2}},\end{aligned}$$

$$\begin{aligned}N_{\varsigma_2\varsigma_2}=\eta_{15}\ \frac{\partial u}{\partial \varsigma_2}+\frac{\eta_{16}}{R_{\varsigma_1}}\frac{\partial u}{\partial \varsigma_2}+\eta_{16}\ \frac{\partial \psi_{\varsigma_1}}{\partial \varsigma_2}+\eta_{15}\ \frac{\partial v}{\partial \varsigma_1}+\frac{\eta_{16}}{R_{\varsigma_2}}\frac{\partial v}{\partial \varsigma_1}\\ +\eta_{16}\ \frac{\partial \psi_{\varsigma_2}}{\partial \varsigma_1},\end{aligned}$$

$$\begin{aligned}M_{\varsigma_1\varsigma_1}=\eta_2\ \frac{\partial u}{\partial \varsigma_1}+\eta_3\ \frac{\partial \psi_{\varsigma_1}}{\partial \varsigma_1}+\frac{\eta_2 w}{R_{\varsigma_1}}+\eta_5\ \frac{\partial v}{\partial \varsigma_2}+\eta_6\ \frac{\partial \psi_{\varsigma_2}}{\partial \varsigma_2}\\ +\frac{\eta_5 w}{R_{\varsigma_2}},\end{aligned}$$

$$\begin{aligned}M_{\varsigma_2\varsigma_2}=\eta_8\ \frac{\partial u}{\partial \varsigma_1}+\eta_9\ \frac{\partial \psi_{\varsigma_1}}{\partial \varsigma_1}+\frac{\eta_8 w}{R_{\varsigma_1}}+\eta_{11}\ \frac{\partial v}{\partial \varsigma_2}+\eta_{12}\ \frac{\partial \psi_{\varsigma_2}}{\partial \varsigma_2}\\ +\frac{\eta_{11} w}{R_{\varsigma_2}},\end{aligned}$$

$$\begin{aligned}M_{\varsigma_2\varsigma_2}=\eta_{16}\ \frac{\partial u}{\partial \varsigma_2}+\frac{\eta_{17}}{R_{\varsigma_1}}\frac{\partial u}{\partial \varsigma_2}+\eta_{17}\ \frac{\partial \psi_{\varsigma_1}}{\partial \varsigma_2}+\eta_{16}\ \frac{\partial v}{\partial \varsigma_1}+\frac{\eta_{17}}{R_{\varsigma_2}}\frac{\partial v}{\partial \varsigma_1}\\ +\eta_{17}\ \frac{\partial \psi_{\varsigma_2}}{\partial \varsigma_1},\end{aligned}$$

$$Q_{\varsigma_1}=\frac{\kappa_s\eta_{13}u}{R_{\varsigma_1}}+\kappa_s\ \eta_{13}\ \psi_{\varsigma_1}+\kappa_s\eta_{13}\ \frac{\partial w}{\partial \varsigma_1},$$

$$Q_{\varsigma_2}=\frac{\kappa_s\eta_{14}v}{R_{\varsigma_2}}+\kappa_s\ \eta_{14}\ \psi_{\varsigma_2}+\kappa_s\ \eta_{14}\ \frac{\partial w}{\partial \varsigma_2}$$

The shear correction factor of FSDT is shown by κ_s in the above stress resultants.

4. Solution procedure

4.1. Navier's method implementation

Among the different solution methods, an analytical approach based on the Fourier series functions which are also recognized as Navier's method is nominated due to its precision. Navier's technique is hired to define displacement components that satisfy the boundary condition of simply supported ends shells. Hence, the displacement can be represented as follows [73]:

$$\begin{Bmatrix}u\\ v\\ w\\ \psi_{\varsigma_1}\\ \psi_{\varsigma_2}\end{Bmatrix}=\sum_{m=1}^{\infty}\sum_{n=1}^{\infty}\begin{Bmatrix}\bar{u}\cos(\mathrm{A}\varsigma_1)\sin(\mathrm{B}\varsigma_2)\\ \bar{v}\sin(\mathrm{A}\varsigma_1)\cos(\mathrm{B}\varsigma_2)\\ \bar{w}\sin(\mathrm{A}\varsigma_1)\sin(\mathrm{B}\varsigma_2)\\ \bar{\psi}_{\varsigma_1}\cos(\mathrm{A}\varsigma_1)\sin(\mathrm{B}\varsigma_2)\\ \bar{\psi}_{\varsigma_2}\sin(\mathrm{A}\varsigma_1)\cos(\mathrm{B}\varsigma_2)\end{Bmatrix} \tag{44}$$

where:

$$\mathrm{A}=\frac{m\pi}{L},\quad \mathrm{B}=\frac{n\pi}{W} \tag{45}$$

The axial and circumferential wavenumbers are depicted by m and n, respectively.

4.2. Mechanical buckling analysis

Finally, using Eq. (44), and substituting its functions into the equations and setting the mechanical in-plane load as $-P_{cr}$, an eigenvalue problem is obtained which its non-trivial answers are the CBLs:

$$\left([K_e]+P_{cr}[K_g]\right)\{X\}=0, \tag{46}$$

in which $[K_e]$ is the stiffness matrix and $[K_g]$ is the geometric stiffness matrix. Also, {X} is the displacement vector.

4.3. Thermal buckling analysis

Parallel to the previous sub-section, the below eigenvalue problem is reached that its non-trivial answers are the critical buckling temperature (CBTs):

$$\left([K_e] + N^T[K_T]\right)\{X\} = 0, \tag{47}$$

Here, the matrix $[K_e]$ represents the elastic stiffness due to mechanical loads, while the matrix $[K_T]$ represents the geometrical stiffness due to temperature variations. The stiffness matrix arrays are presented in the Appendix section for reference.

Table 1. Comparing the CBLs of a cylindrical shell with different *L/h* ratio with previously published works.

L/h	Ref. [74]	Ref. [75]	Ref. [76]	Present
10	2.9533	2.9718	2.9602	2.9618
20	1.6801	1.6831	1.6804	1.6807
30	1.2876	1.2817	1.2787	1.2797
40	1.1418	1.1127	1.1185	1.1179

Table 2. Comparison of the first four CBLs of a cylindrical shell with different material gradient index (γ) values.

		Material gradient index (γ)						
(*m*, *n*)	Source	0	0.5	1	2	5	10	20
(1, 1)	Ref. [77]	1.2768	1.0390	0.9313	0.8366	0.7464	0.6933	0.6525
	Ref. [76]	1.3059	1.0496	0.9356	0.8377	0.7473	0.6971	0.6576
	Present	1.2986	1.0459	0.9321	0.8373	0.7470	0.6958	0.6547
(2, 1)	Ref. [77]	1.4098	1.1314	1.0149	0.9217	0.8377	0.7812	0.7324
	Ref. [76]	1.4763	1.1762	1.0489	0.9476	0.8324	0.7743	0.7338
	Present	1.4503	1.1611	1.0394	0.9396	0.8312	0.7704	0.7317
(1, 2)	Ref. [77]	1.5149	1.2509	1.1241	1.0043	0.8828	0.8153	0.7677
	Ref. [76]	1.4819	1.1980	1.0675	0.9500	0.8642	0.8092	0.7588
	Present	1.4962	1.2003	1.0786	0.9649	0.8691	0.8106	0.7594
(2, 2)	Ref. [77]	1.8434	1.4683	1.3175	1.2042	1.1061	1.0334	0.9666
	Ref. [76]	1.8258	1.4407	1.2850	1.1700	1.0739	1.0072	0.9421
	Present	1.8314	1.4496	1.2923	1.1784	1.0806	1.0118	0.9479

Table 3. Material properties of the structure [78].

Properties	Porous core (SUS304)	GPLs reinforcement	Epoxy matrix
E (GPa)	201.04×10^3	1.01×10^3	130
ρ (kg/m^3)	8166	1062.5	8960
N	0.3262	0.186	0.34
α ($\times 10^{-6}$K^{-1})	12.33	2.35	8.2
w (μm)	–	1.5	–
h (nm)	–	1.5	–
l (μm)	–	2.5	–

5. Results and discussion

5.1. Results' authentication

The opening phase in presenting the outcomes of the current work is authorizing their exactness. It can be reached by comparing them in simpler cases with prior published studies. Hence, the dimensionless CBLs of a cylindrical shell are attained and tabulated in Table 1. As shown in the table, the findings of this study are consistent with the outcomes reported by Tan et al. [74], Huan et al. [75], and Cuong-Le et al. [76]. The results of this table are achieved for an FG cylindrical shell which is made from Al/ZrO2-3, which its relations are presented in Ref. [76] and the numerical values of its mechanical properties are as follows: $E_c = 151$ GPa, $\nu_c = 0.3$, $\rho_c = 3000$ kg/m^3, $E_m = 70$ GPa, $\nu_m = 0.3$, and $\rho_m = 2707$ kg/m^3. The results are presented for different values of *L/h* ratio and a bit of difference with the reference studies may be raised from different used shear deformation theory or solution approaches. Also, it should be noted that the results can be obtained for a cylindrical shell by tending R_{ς_2} to infinity and the dimensionless CBL is achieved *via* $P^*_{cr} = P_{cr}\frac{R_{\varsigma_1}}{E_m h^2}$. Therefore, in this phase the results reliability is confirmed. As the second effort for checking the results, Table 2 presents the dimensionless CBLs for first four buckling modes of an FG cylindrical shell for various material gradient indices. Another time, it is seen a good merging between the existing results and those of Zhao and Liew [77] and Cuong-Le et al. [76]. The dimensionless CBL in this table has the same definition as Table 1. So, the results' precision is guaranteed.

5.2. Case study

5.2.1. Mechanical buckling results

The dimensionless CBL can be gained by reaching the non-trivial answers of Eq. (46). Remarkably, Table 3 presents the material properties of the shell [78]. Also, the subsequent values and specifications are used to extract the outcomes: $\beta = 0.25$, $B = 0.2$, $h = 2$ cm, $h_t = h_b = 0.1h_c$, $a = 10h$, $b = a$, $V^*_{GPL} = 0.5\%$, Type B and Uniform patterns for imperfection and GPLs' dispersion, respectively. Noted that the dimensionless CBL is defined as $P^*_{cr} = P_{cr}\frac{(1-\nu^2)}{Eh}$. Table 4 explores

Table 4. Effect of imperfection type and ratio and also, different values of Skempton coefficient on the dimensionless CBLs of different types of shell.

		Imperfection ratio ($\beta = 0.2$)				Imperfection ratio ($\beta = 0.5$)			
		Skempton coefficient				Skempton coefficient			
Shell type	Imperfection type	0.0	0.2	0.4	0.6	0.0	0.2	0.4	0.6
Cylindrical	A	9.3802	9.4351	9.4889	9.5418	7.3141	7.4184	7.5180	7.6133
	B	9.7519	9.8082	9.8635	9.9177	8.4125	8.5225	8.6280	8.7293
	C	9.2975	9.3890	9.4787	9.5666	7.1438	7.3220	7.4915	7.6530
Spherical	A	15.3694	15.4287	15.4870	15.5445	12.0092	12.1172	12.2215	12.3221
	B	15.7401	15.8293	15.9161	16.0007	13.1043	13.2719	13.4298	13.5791
	C	15.2680	15.3941	15.5171	15.6372	11.7003	11.9450	12.1748	12.3912
Doubly-Curved	A	11.8857	11.9400	11.9934	12.0461	9.2769	9.3782	9.4758	9.5697
	B	12.2582	12.3282	12.3966	12.4635	10.3773	10.5113	10.6386	10.7599
	C	11.7958	11.9017	12.0052	12.1065	9.0505	9.2564	9.4510	9.6353

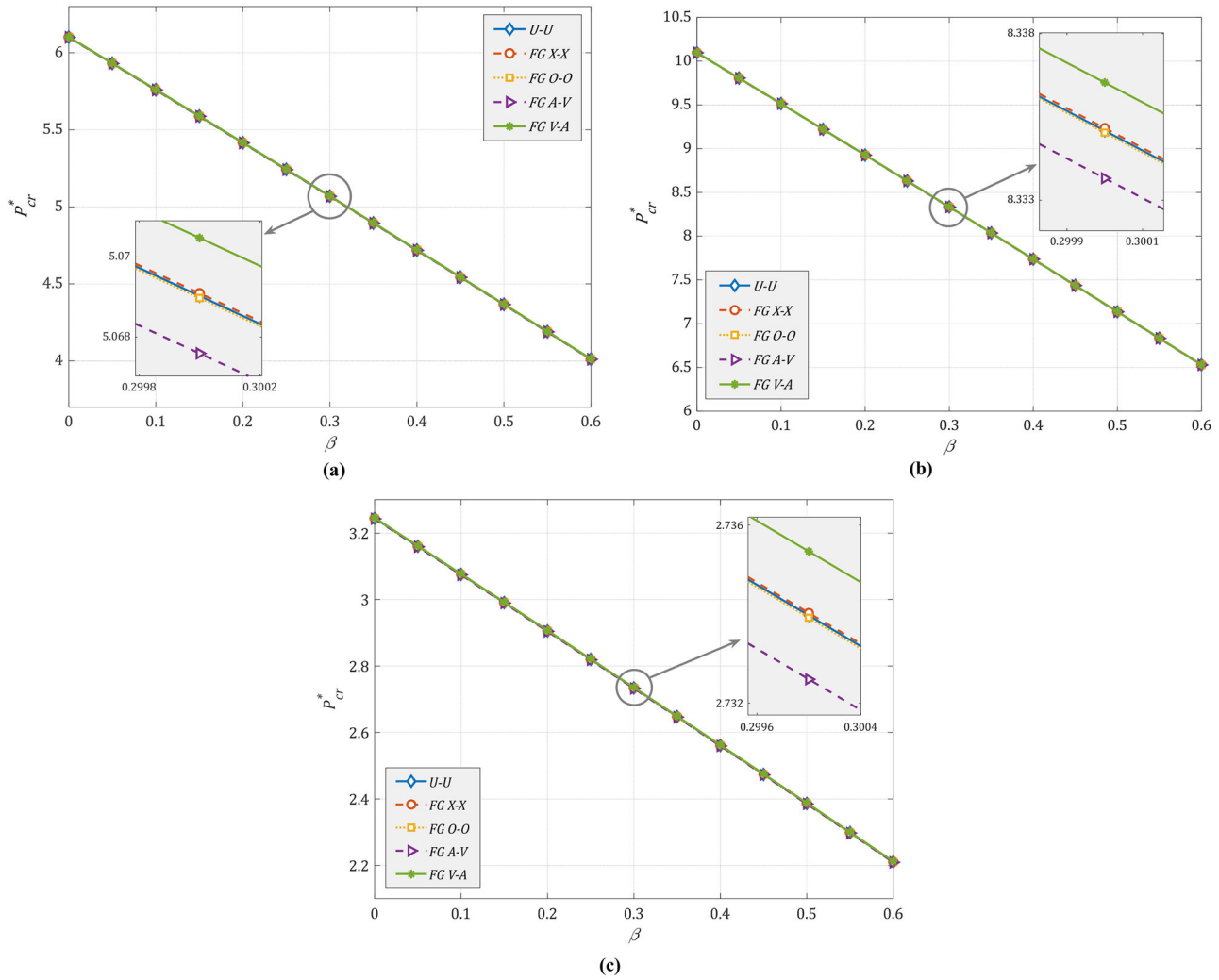


Figure 2. Effects of imperfection ratio and different patterns of GPLs' dispersion on dimensionless CBL of the (a) doubly-curved; (b) spherical; and (c) cylindrical shell.

Table 5. Dimensionless CBLs for different types of shell.

	(*m*, *n*)								
Shell Type	(1)	(1, 2)	(1, 2)	(2)	(1, 3)	(1, 3)	(2, 3)	(2, 3)	(3)
Cylindrical	9.4039	19.7233	17.9367	27.4005	33.7141	32.5258	40.6631	40.2285	51.4532
Spherical	15.0149	20.8051	20.8051	28.8026	34.0036	34.0036	41.2661	41.2661	52.0757
Doubly-curved	11.7525	20.2393	18.8993	27.9935	33.8568	32.9655	40.9428	40.6169	51.7194

different parameters' effects on the CBL for three kinds of shells, namely cylindrical, spherical, and doubly-curved. As can be understood, increasing the imperfection ratio which reveals the ratio of pores' volume to that of the whole, tends the CBLs to reduce. In fact, increasing the imperfection ratio, affects the stiffness of the structure and CBL is generally proportional to stiffness, so it reduces. Comparing three different types of imperfection (i.e. Types A, B, and C) displays that Type B leads to the highest values of critical buckling load, while Type C tends the results to the lowest values. As a notice, it should be said that Types B and C were linked to symmetric and uniform patterns of imperfection, separately. It happens for all kinds of considered shells, regardless of their shapes. Furthermore, the effect of the Skempton parameter which indicates the pores' pressure is investigated in Table 4. As can be gotten, increasing the Skempton coefficient leads the results to enhance, due to enhancement in the structure's stiffness. And as the last finding of this table, it is seen that the CBLs of the spherical shell are more than two other kinds of shells and those of cylindrical shells are the least ones. In Figure 2, the effects of GPLs' dispersion patterns and imperfection ratio increasing on the dimensionless CBL are investigated for all three kinds of considered shells, namely cylindrical, spherical, and doubly-curved. As can be found, FG V-A and FG A-V patterns cause the most and the least values of critical buckling load, respectively. It occurs due to nano-fillers' dispersion in the surfaces. It means as the amount of nano-fillers in the surfaces becomes more than the mid-surface, the stiffness of the structure enhances. Moreover, Figure 2 confirms the previous findings about the impact of the imperfection ratio on the results. The dimensionless CBLs for different values of axial and circumferential wavenumbers are listed in Table 5. As can be expected, the spherical shell has the most

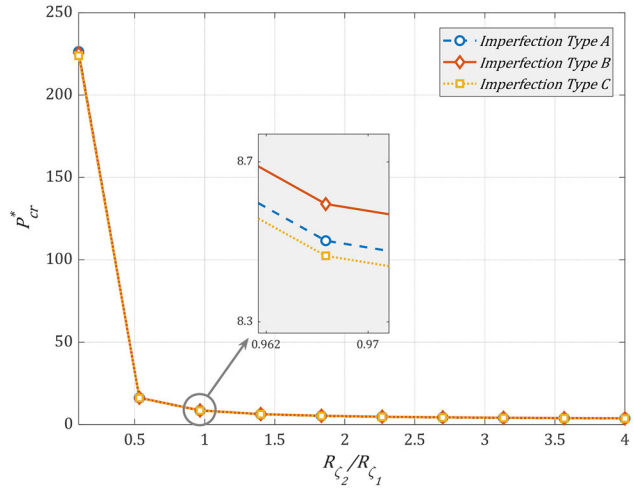


Figure 3. Effects of curvature radii ratio and imperfection patterns of the core on dimensionless CBL of the structure.

Table 6. The CBLs of cylindrical shell with different material geometrical properties and GPL's total mass fraction percentage.

		V^*_{GPL} (%)				
L/h	$R_{\zeta 1}$/L	0	0.5	1	1.5	2
10	2	9.2075	9.3847	9.5617	9.7387	9.9155
	3	8.2005	8.3713	8.5419	8.7125	8.8829
	5	7.6847	7.8522	8.0196	8.1868	8.3540
	10	7.4670	7.6332	7.7992	7.9650	8.1308
	20	7.4126	7.5784	7.7441	7.9096	8.0750
	50	7.3974	7.5631	7.7286	7.8941	8.0594
30	2	2.7021	2.7340	2.7659	2.7978	2.8298
	3	1.6744	1.6995	1.7246	1.7497	1.7748
	5	1.1483	1.1698	1.1914	1.2130	1.2346
	10	0.9263	0.9464	0.9665	0.9866	1.0067
	20	0.8708	0.8905	0.9103	0.9300	0.9497
	50	0.8553	0.8749	0.8945	0.9141	0.9337

values of critical buckling load, while the cylindrical shell has the least ones. The effects of the curvature radii ratio and imperfection patterns of the porous core on the results are studied in Figure 3. Regarding this figure, it is seen that as the curvature radii ratio increases, the CBL reduces significantly owing to a dump in model's stiffness. Also, it is observed that imperfection Type B leads to the highest values of CBL and Type C leads to the least ones. The effects of three parameters are considered in Tables 6–8. The first effect is related to the GPLs' total mass fraction percentage. Since the GPLs' stiffness is high, so adding even a small amount of them will enhance the structure's stiffness meaningfully. Therefore, the normalized CBLs increase. Also, it is seen as the length to the whole thickness of the shell ratio enhances, the CBLs reduce owed to the drop in structure's stiffness. And as the last finding from Tables 6–8, it is observed that an increment in $R_{\zeta 1}/L$, leads the results to reduce. It is important to mention that the outcomes presented in Tables 6–8 correspond to cylindrical, spherical, and doubly-curved shells, respectively. In Figure 4, in addition to seeing GPLs' total mass fraction, the effect of different kinds of elastic substrate is also considered. In the case of substrate-free, the results are in their lowest values, but adding a single layer of springs which is known as Winkler substrate, rises the structure's rigidity that leads to

Table 7. The CBLs of spherical shell with different material geometrical properties and GPL's total mass fraction percentage.

		V^*_{GPL} (%)				
L/h	$R_{\zeta 1}$/L	0	0.5	1	1.5	2
10	2	14.7706	14.9850	15.1993	15.4136	15.6278
	3	10.6731	10.8604	11.0477	11.2348	11.4218
	5	8.5749	8.7483	8.9217	9.0949	9.2680
	10	7.6896	7.8572	8.0247	8.1921	8.3593
	20	7.4683	7.6344	7.8005	7.9663	8.1321
	50	7.4063	7.5721	7.7377	7.9031	8.0685
30	2	8.2659	8.3351	8.4043	8.4736	8.5430
	3	4.1473	4.1889	4.2306	4.2723	4.3140
	5	2.0385	2.0660	2.0936	2.1211	2.1487
	10	1.1488	1.1704	1.1920	1.2136	1.2352
	20	0.9264	0.9465	0.9666	0.9867	1.0068
	50	0.8642	0.8838	0.9035	0.9232	0.9429

Table 8. The CBLs of doubly-curved shell with different material geometrical properties and GPL's total mass fraction percentage.

		V^*_{GPL} (%)				
L/h	$R_{\zeta 1}$/L	0	0.5	1	1.5	2
10	2	11.5359	11.7289	11.9217	12.1144	12.3070
	3	9.2353	9.4131	9.5908	9.7683	9.9458
	5	8.0572	8.2273	8.3972	8.5669	8.7366
	10	7.5602	7.7269	7.8936	8.0601	8.2264
	20	7.4359	7.6019	7.7677	7.9333	8.0989
	50	7.4011	7.5668	7.7324	7.8979	8.0632
30	2	5.0216	5.0690	5.1165	5.1641	5.2116
	3	2.7053	2.7373	2.7693	2.8013	2.8334
	5	1.5194	1.5435	1.5675	1.5916	1.6157
	10	1.0191	1.0398	1.0605	1.0812	1.1019
	20	0.8940	0.9139	0.9338	0.9536	0.9735
	50	0.8590	0.8786	0.8983	0.9179	0.9376

enhancement in CBLs. Also, adding a shear layer to the springs converts the substrate type to Pasternak one which again, increases the CBLs. Figure 5 shows how the CBL of GPLs is affected by their geometric parameters. The results demonstrate that an increase in the height-to-length ratio of GPLs contributes to a notable reduction in the outcomes. This occurs because the stiffness of GPLs decreases, ultimately affecting the overall stiffness of the structure. A similar effect is also seen with the length-to-width ratio of GPLs. Figure 6 provides a comprehensive judgment of the CBLs for different kinds of shells, showing that cylindrical and doubly-curved shells have the uppermost and lowermost values of CBLs, one-to-one (Figure 7).

5.2.2. Thermal buckling results

Now, it turns to consider the thermal buckling analysis results. The specifications of the under-evaluation model are the same as those mentioned in the mechanical buckling analysis. It should be mentioned that the changes in dimensionless CBT are defined as $\Delta T^*_{cr} = \Delta T_{cr} \frac{(1-\nu^2)}{\alpha h}$. Figure 8 investigates the impact of two parameters related to the porous core, namely the type of imperfection and the imperfection ratio, on the CBT of the model being studied. It is seen that increasing the imperfection ratio, contrary to expectations, enhances the CBT. A similar effect about porous structures is seen in Refs. [79, 80]. Also, among the three types of imperfections, the impact of the imperfection type and imperfection ratio on the CBT of the model under

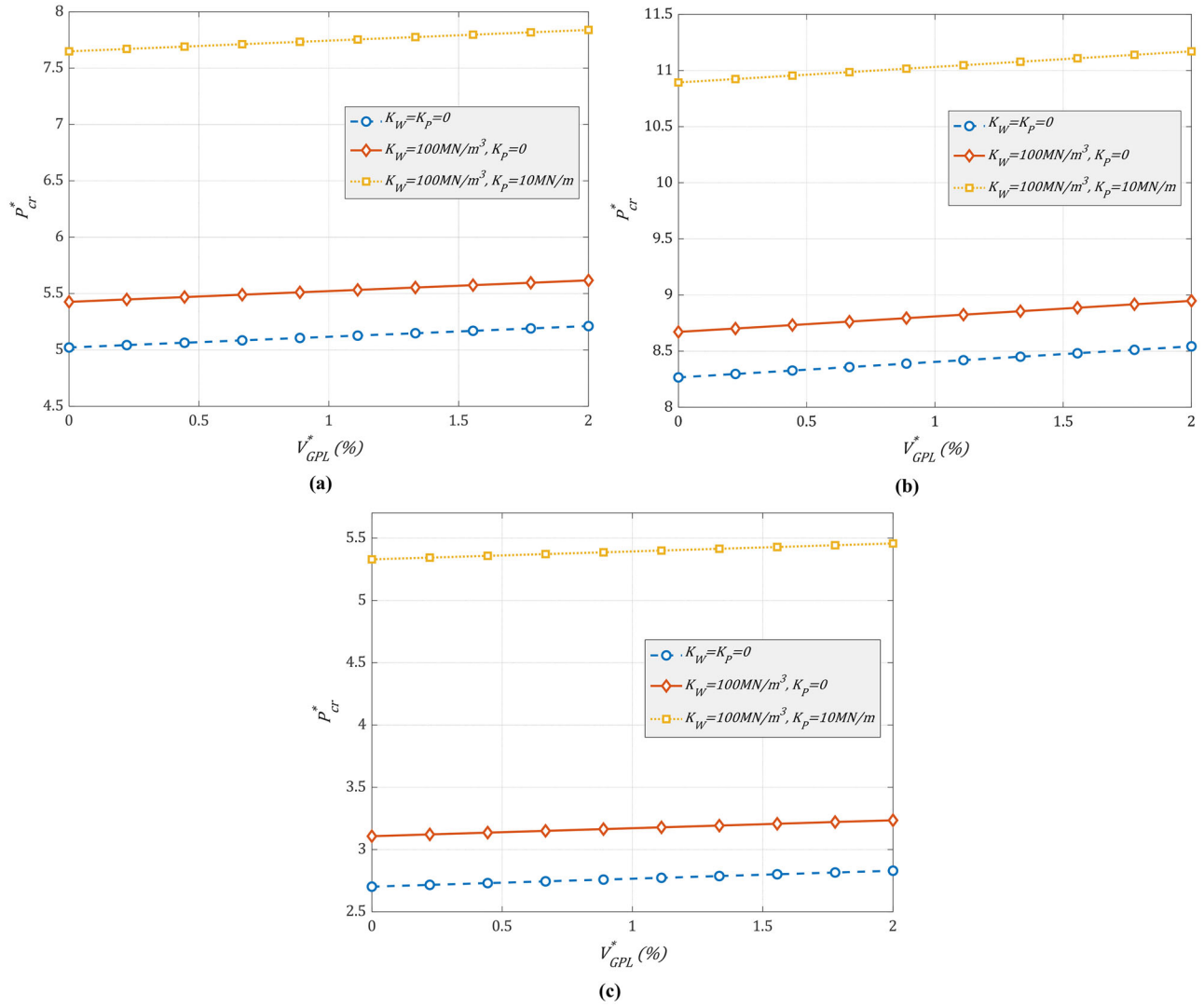


Figure 4. Effects of GPLs' total mass fraction and different kinds of elastic substrate on dimensionless CBL of the (a) doubly-curved; (b) spherical; and (c) cylindrical shell.

consideration is illustrated in Figure 8. The results indicate that imperfection Type A results in the lowest CBT, while Types B and C produce similar results. Additionally, the effect of the total mass fraction of GPLs on the CBT is examined in Figure 8 for different shell types. As can be found, increasing the nano-fillers total mass fraction, reduces the CBT slightly. A similar result is seen in Refs. [78, 80, 81]. So, it can be one of the most prominent results of this work. In Tables 9–11, the effects of GPLs' geometrical parameters, their dispersion patterns, and also the Skempton coefficient on the CBT for respectively, cylindrical, spherical, and doubly-curved shells are evaluated. As the length-to-width ratio of GPLs increases, the CBT decreases. However, this alteration is not significant. Besides, it is observed that the results due to FG V-A and FG A-V cases are the maximum and minimum CBTs, individually. And an increment in the Skempton coefficient leads the CBTs to reduce. It occurs due to changes in the structure's thermal stiffness. A comparison between different kinds of shells versus the curvature radius to length ratio is provided in Figure 9. Based on this figure, the cylindrical shell has the smallest values of CBT and doubly-curved shell has the highest values. Moreover, as the curvature radius to length ratio increases, the CBT tends to decrease. In Figure 10, another GPLs' geometrical parameter is taken into the investigation: height-to-length ratio. According to the results shown in the figure, a slight enhancement in the CBT can be observed when the height-to-length ratio of GPLs reinforcements is raised. Additionally, the observation is that the CBT decreases significantly as the curvature radii increase. The study also analyzes how the parameters of the substrate have an impact on the CBT. As anticipated, the CBT increases when both of these parameters are increased. This is due to a rise in the stiffness of the structure. Finally, in Table 12, the CBTs for different values of axial and circumferential wavenumbers are presented for various types of shells (Figure 11).

6. Conclusions

In this paper, thermo-mechanical buckling act of three-layered advanced fluid-infiltrated porous shells that are embedded between two GPLs-reinforced composite layers is

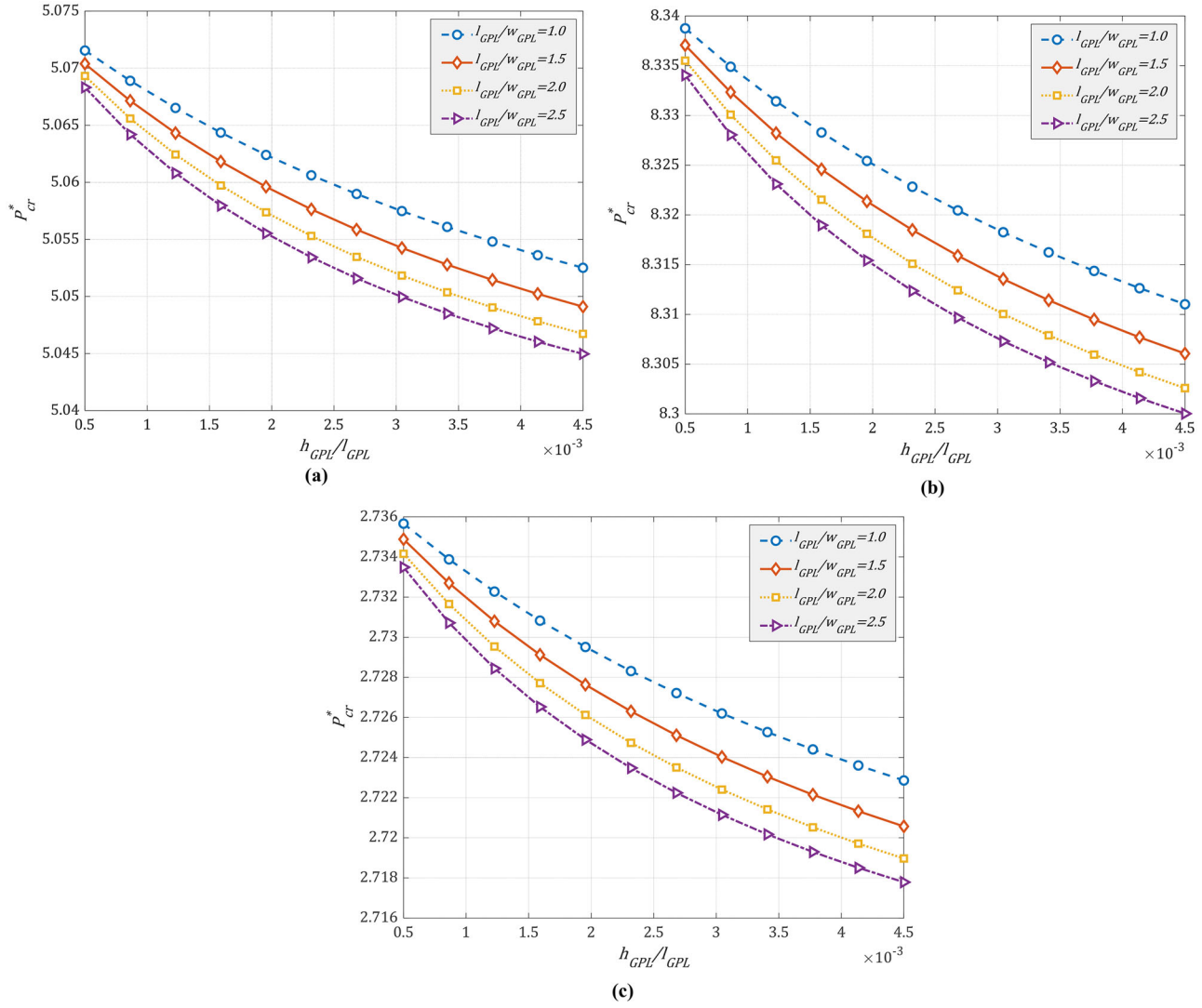


Figure 5. Effects of GPLs' geometrical specifications on dimensionless CBL of the (a) doubly-curved; (b) spherical; and (c) cylindrical shell.

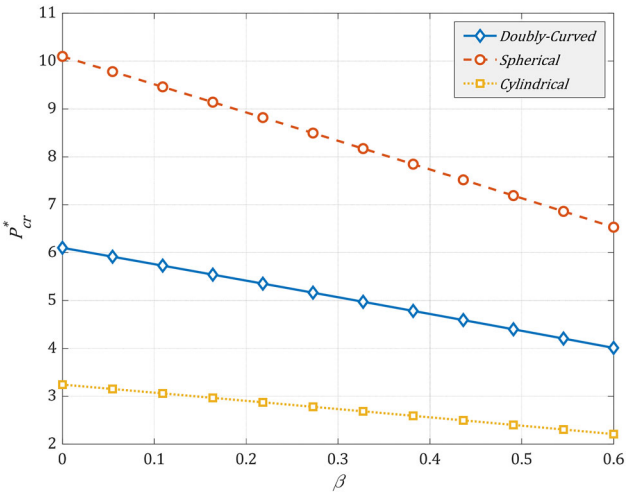


Figure 6. Comparing dimensionless CBL of different types of curved structures versus the core's imperfection ratio.

examined. The results are obtained *via* Navier's approach and their correctness is assured by comparing them with formerly published works. Lastly, the impression of different factors on the CBLs and CBTs of cylindrical, spherical, and doubly-curved shells is analyzed and the below items are concluded:

- Increasing the imperfection ratio reduces the critical buckling load, but enhances the CBT. Among the considered imperfection patterns, type B which relates to the symmetric pattern has the most values of CBL and those of types A and B were close to each other. Also, for CBT, the results due to type A are the minimum ones.
- Enhancing the GPLs' total mass fraction, rises and lessens the CBL and CBTs, respectively. Moreover, linking different types of GPLs' dispersion patterns shows that the FG V-A and FG A-V patterns have the uppermost and the lowermost values of results in both thermal and mechanical buckling analyses, respectively.
- When the Skempton coefficient, which represents the pressure in pores, is increased, the CBL is found to rise, while the CBT decreases.
- Geometrical parameters of GPLs play a crucial role in both mechanical and thermal buckling analyses.

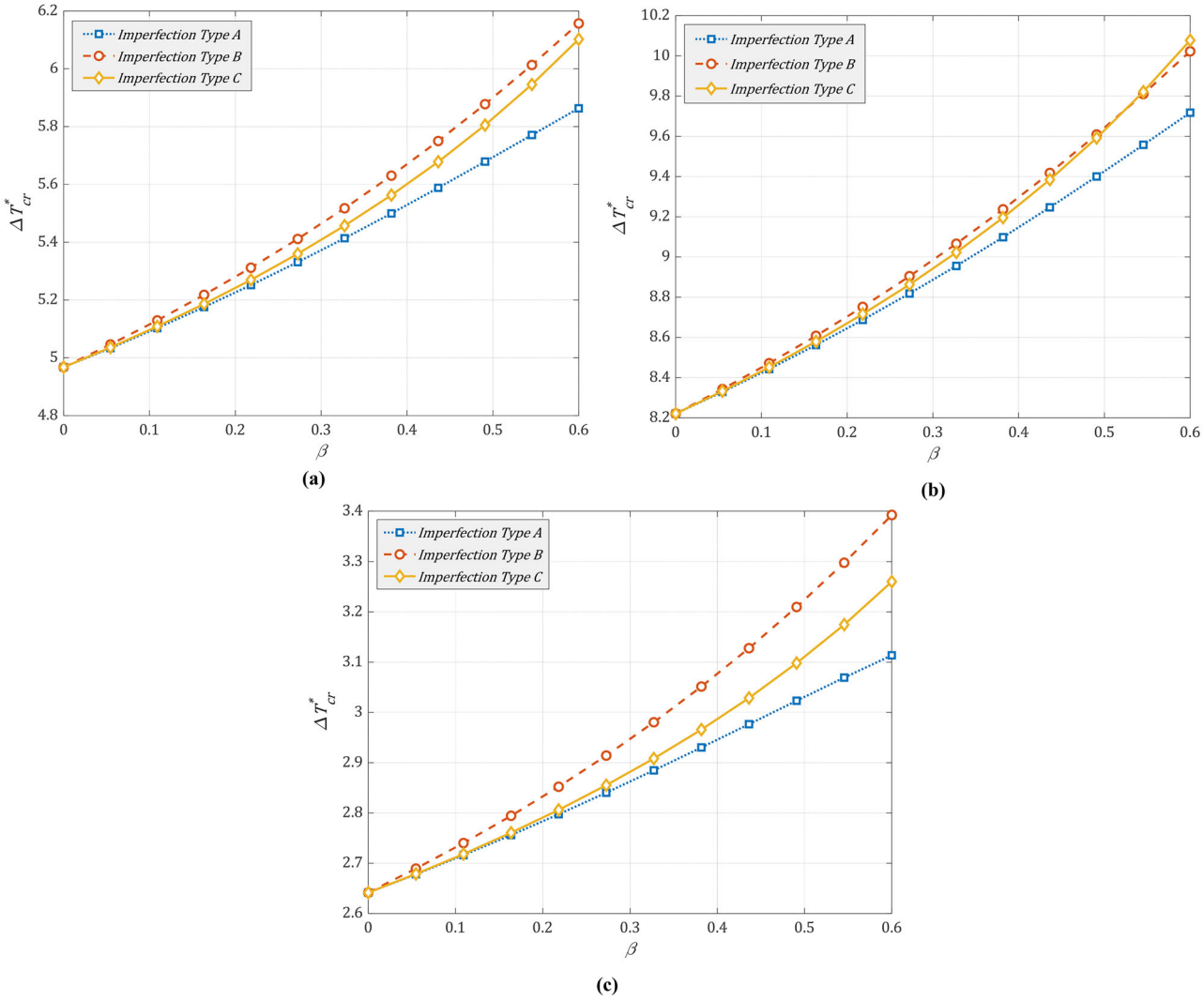


Figure 7. Effects of imperfection ratio and different patterns of imperfection on dimensionless CBT of the (a) doubly-curved; (b) spherical; and (c) cylindrical shell.

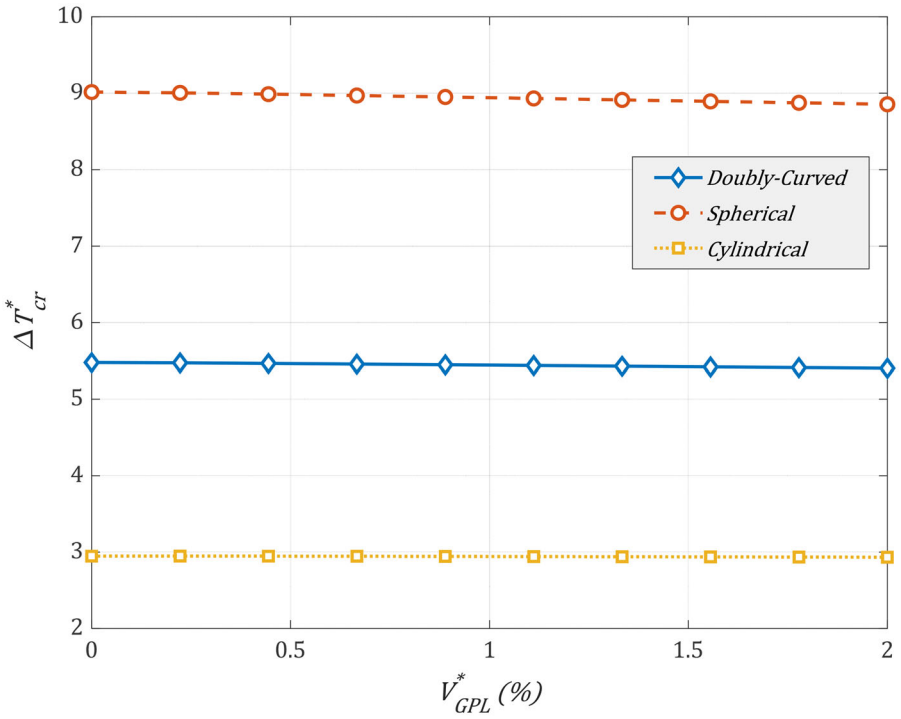


Figure 8. Comparing dimensionless CBT of different types of curved structures versus the GPLs' total mass fraction.

Table 9. Effect of GPLs' length-to-width ratio and dispersion patterns, and Skempton coefficient on the CBTs of cylindrical shell.

GPLs disp.	$l_{GPLs} = w_{GPLs}$ Skempton coefficient 0.0	0.2	0.4	0.6	$l_{GPLs} = 2\ w_{GPLs}$ Skempton coefficient 0.0	0.2	0.4	0.6
U-U	10.2598	10.1167	9.9835	9.8593	10.2576	10.1146	9.9816	9.8575
X-X	10.2580	10.1149	9.9818	9.8576	10.2561	10.1132	9.9802	9.8562
O-O	10.2572	10.1142	9.9811	9.8569	10.2553	10.1124	9.9795	9.8554
A-V	10.2446	10.1019	9.9691	9.8451	10.2424	10.0998	9.9671	9.8433
V-A	10.2705	10.1272	9.9938	9.8694	10.2690	10.1258	9.9926	9.8682
X-O	10.2576	10.1146	9.9814	9.8573	10.2557	10.1128	9.9798	9.8558
O-X	10.2576	10.1146	9.9814	9.8573	10.2557	10.1128	9.9798	9.8558
V-V	10.2576	10.1146	9.9814	9.8572	10.2558	10.1128	9.9798	9.8557
A-A	10.2575	10.1145	9.9815	9.8573	10.2557	10.1128	9.9799	9.8558

Table 10. Effect of GPLs' length-to-width ratio and dispersion patterns, and Skempton coefficient on the CBTs of spherical shell.

GPLs disp.	$l_{GPLs} = w_{GPLs}$ Skempton coefficient 0.0	0.2	0.4	0.6	$l_{GPLs} = 2\ w_{GPLs}$ Skempton coefficient 0.0	0.2	0.4	0.6
U-U	16.3868	16.1556	15.9389	15.7355	16.3811	16.1501	15.9337	15.7306
X-X	16.3836	16.1525	15.9359	15.7327	16.3785	16.1476	15.9314	15.7283
O-O	16.3828	16.1517	15.9352	15.7319	16.3777	16.1469	15.9306	15.7276
A-V	16.3703	16.1394	15.9232	15.7202	16.3648	16.1342	15.9182	15.7155
V-A	16.3962	16.1648	15.9480	15.7444	16.3914	16.1603	15.9437	15.7404
X-O	16.3832	16.1521	15.9356	15.7323	16.3781	16.1473	15.9310	15.7279
O-X	16.3832	16.1521	15.9356	15.7323	16.3781	16.1472	15.9310	15.7279
V-V	16.3833	16.1521	15.9355	15.7322	16.3782	16.1473	15.9309	15.7278
A-A	16.3831	16.1521	15.9356	15.7324	16.3780	16.1472	15.9310	15.7280

Table 11. Effect of GPLs' length-to-width ratio and dispersion patterns, and Skempton coefficient on the CBTs of doubly-curved shell.

GPLs disp.	$l_{GPLs} = w_{GPLs}$ Skempton coefficient 0.0	0.2	0.4	0.6	$l_{GPLs} = 2\ w_{GPLs}$ Skempton coefficient 0.0	0.2	0.4	0.6
U-U	12.8246	12.6445	12.4763	12.3188	12.8208	12.6410	12.4730	12.3157
X-X	12.8221	12.6421	12.4740	12.3166	12.8189	12.6391	12.4712	12.3140
O-O	12.8214	12.6414	12.4733	12.3159	12.8181	12.6383	12.4704	12.3132
A-V	12.8088	12.6291	12.4612	12.3041	12.8052	12.6257	12.4580	12.3011
V-A	12.8347	12.6544	12.4860	12.3284	12.8319	12.6518	12.4835	12.3261
X-O	12.8217	12.6417	12.4736	12.3163	12.8185	12.6387	12.4708	12.3136
O-X	12.8217	12.6417	12.4736	12.3163	12.8185	12.6387	12.4708	12.3136
V-V	12.8218	12.6418	12.4736	12.3162	12.8186	12.6387	12.4707	12.3135
A-A	12.8217	12.6417	12.4737	12.3164	12.8184	12.6387	12.4708	12.3137

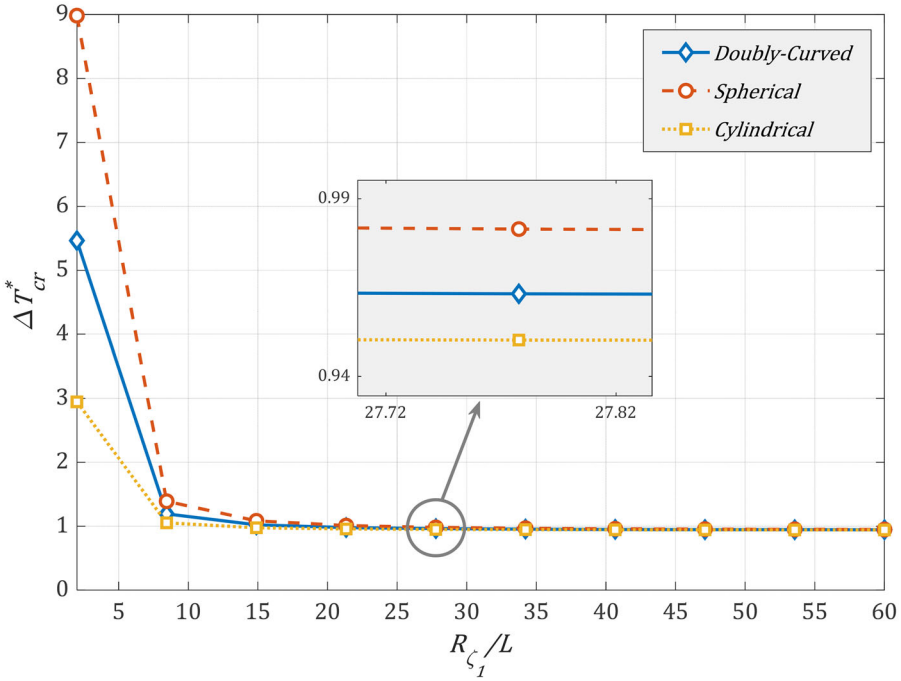


Figure 9. Comparing dimensionless CBT of different types of curved structures versus the curvature radius to length ratio.

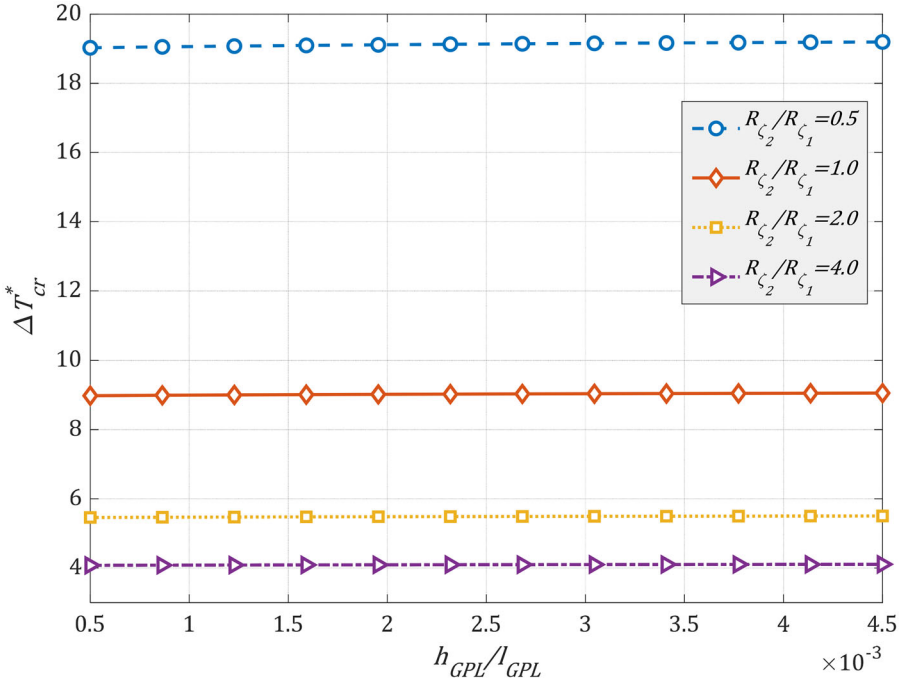


Figure 10. Effects of GPLs' and structure's geometrical specifications on dimensionless CBT.

Table 12. Dimensionless CBTs for different types of shell.

	(*m*, *n*)								
Shell type	(1)	(1, 2)	(1, 2)	(2)	(1, 3)	(1, 3)	(2, 3)	(2, 3)	(3)
Cylindrical	10.1151	21.2169	19.2950	29.4786	36.2733	34.9949	43.7537	43.2863	55.3714
Spherical	16.1513	22.3808	22.3808	30.9870	36.5848	36.5848	44.4025	44.4025	56.0410
Doubly-curved	12.6417	21.7721	20.3306	30.1166	36.4268	35.4680	44.0547	43.7041	55.6577

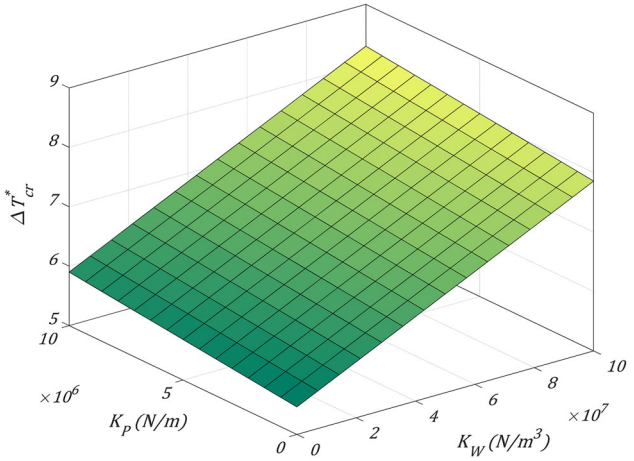


Figure 11. Influence of elastic substrate parameters on the dimensionless CBT of the doubly-curved panel..

- The results due to cylindrical shells are generally fewer than those of spherical shells.
- The addition of an elastic substrate, regardless of its composition, results in an increase in both CBLs and CBTs.
- Enhancement in curvature radius to length ratio reduces both CBLs and CBTs.
- As the length-to-height ratio of the structure becomes more, the results tend to reduce.

Disclosure statement

The authors state that there is no conflict of interest for them to disclose.

ORCID

Ehsan Arshid http://orcid.org/0000-0002-7731-7386
Abhinav Kumar http://orcid.org/0000-0003-1777-7994

References

[1] M. Esfandiari, H. Haghighi, and G. Urgessa, Machine learning-based optimum reinforced concrete design for progressive collapse, EJSE, vol. 23, no. 2, pp. 1–8, 2023. DOI: 10.56748/ejse.233642.

[2] M. Izadifar, N. Luo, M.Y. Abu-Farsakh, and S. Chen, Performance evaluation of design methods for geosynthetic-reinforced pile-supported embankments, Transp. Res. Rec. J. Transp. Res. Board., 2023. DOI: 10.1177/03611981231165994.

[3] M. Afzali, M. Farrokh, and E. Carrera, Nonlinear thermal post-buckling analysis of rectangular FG plates using CUF, Compos. Struct., vol. 321, p. 117282, 2023. DOI: 10.1016/j.compstruct.2023.117282.

[4] Z.-Z. Wang, T. Wang, Y. Ding, and L. Ma, A simple refined plate theory for the analysis of bending, buckling and free vibration of functionally graded porous plates reinforced by graphene platelets, Mech. Adv. Mater. Struct., pp. 1–18, 2022. DOI: 10.1080/15376494.2022.2141383.

[5] S. Amir, E.M.R. Bidgoli, and E. Arshid, Size-dependent vibration analysis of a three-layered porous rectangular nano plate

with piezo-electromagnetic face sheets subjected to pre loads based on SSDT, Mech. Adv. Mater. Struct., vol. 27, no. 8, pp. 605–619, 2020. DOI: 10.1080/15376494.2018.1487612.

[6] E. Detournay, and A.H.-D. Cheng, Fundamentals of poroelasticity, Anal. Des. Methods, pp. 113–171, 1993. DOI: 10.1016/B978-0-08-040615-2.50011-3.

[7] V. Farhangi, M. Zadehmohamad, A. Monshizadegan, M.A. Izadifar, M.J. Moradi, and H. Dabiri, Effects of geogrid reinforcement on the backfill of integral bridge abutments, Buildings., vol. 13, no. 4, pp. 853, 2023. DOI: 10.3390/buildings13040853.

[8] A. Ikbarieh, M.A. Izadifar, M.Y. Abu-Farsakh, and G.Z. Voyiadjis, A parametric study of embankment supported by geosynthetic reinforced load transfer platform and timber piles tip on sand, Transp. Geotech., vol. 38, pp. 100901, 2023. DOI: 10.1016/j.trgeo.2022.100901.

[9] M. Kianezhad, M. Youzi, M. Vaezi, and H. Nejat Pishkenari, Rectilinear motion of carbon nanotube on gold surface, Int. J. Mech. Sci., vol. 217, pp. 107026, 2022. DOI: 10.1016/j.ijmecsci.2021.107026.

[10] N.D. Dat, N. Van Thanh, V. MinhAnh, and N.D. Duc, Vibration and nonlinear dynamic analysis of sandwich FG-CNTRC plate with porous core layer, Mech. Adv. Mater. Struct., vol. 29, no. 10, pp. 1431–1448, 2022. DOI: 10.1080/15376494.2020.1822476.

[11] M. Shakir, M. Talha, and A.D. Dileep, Machine learning based probabilistic model for free vibration analysis of functionally graded graphene nanoplatelets reinforced porous plates, Mech. Adv. Mater. Struct., pp. 1–14, 2023. DOI: 10.1080/15376494.2023.2225051.

[12] M. Kianezhad, M. Youzi, M. Vaezi, and H. Nejat Pishkenari, Unidirectional motion of C60-based nanovehicles using hybrid substrates with temperature gradient, Sci Rep., vol. 13, no. 1, pp. 1100, 2023. DOI: 10.1038/s41598-023-28245-4.

[13] E. Sobhani, A.R. Masoodi, O. Civalek, and A.R. Ahmadi-Pari, Agglomerated impact of CNT vs. GNP nanofillers on hybridization of polymer matrix for vibration of coupled hemispherical-conical-conical shells, Aerosp. Sci. Technol., vol. 120, pp. 107257, 2022. DOI: 10.1016/j.ast.2021.107257.

[14] E. Sobhani, and M. Avcar, The influence of various nanofiller materials (CNTs, GNPs, and GOPs) on the natural frequencies of Nanocomposite Cylindrical Shells: a comparative study, Mater. Today Commun., vol. 33, pp. 104547, 2022. DOI: 10.1016/j.mtcomm.2022.104547.

[15] M.C. Trinh, and S.E. Kim, A three variable refined shear deformation theory for porous functionally graded doubly curved shell analysis, Aerosp. Sci. Technol., vol. 94, pp. 105356, 2019. DOI: 10.1016/j.ast.2019.105356.

[16] C. Zhu, X. Fang, and G. Nie, Nonlinear free and forced vibration of porous piezoelectric doubly-curved shells based on NUEF model, Thin-Walled Struct., vol. 163, pp. 107678, 2021. DOI: 10.1016/j.tws.2021.107678.

[17] J. Zhao, F. Xie, A. Wang, C. Shuai, J. Tang, and Q. Wang, Vibration behavior of the functionally graded porous (FGP) doubly-curved panels and shells of revolution by using a semi-analytical method, Compos. Part B Eng., vol. 157, pp. 219–238, 2019. DOI: 10.1016/j.compositesb.2018.08.087.

[18] A. Wang, H. Chen, Y. Hao, and W. Zhang, Vibration and bending behavior of functionally graded nanocomposite doubly-curved shallow shells reinforced by graphene nanoplatelets, Results Phys., vol. 9, pp. 550–559, 2018. DOI: 10.1016/j.rinp.2018.02.062.

[19] J.J. Mao, and W. Zhang, Linear and nonlinear free and forced vibrations of graphene reinforced piezoelectric composite plate under external voltage excitation, Compos. Struct., vol. 203, pp. 551–565, 2018. DOI: 10.1016/j.compstruct.2018.06.076.

[20] J.J. Mao, and W. Zhang, Buckling and post-buckling analyses of functionally graded graphene reinforced piezoelectric plate subjected to electric potential and axial forces, Compos. Struct., vol. 216, pp. 392–405, 2019. DOI: 10.1016/j.compstruct.2019.02.095.

[21] Y. Wang, and W. Zhang, On the thermal buckling and post-buckling responses of temperature-dependent graphene platelets reinforced porous nanocomposite beams, Compos. Struct., vol. 296, pp. 115880, 2022. DOI: 10.1016/j.compstruct.2022.115880.

[22] R. Talebitooti, and M.R. Zarastvand, The effect of nature of porous material on diffuse field acoustic transmission of the sandwich aerospace composite doubly curved shell, Aerosp. Sci. Technol., vol. 78, pp. 157–170, 2018. DOI: 10.1016/j.ast.2018.03.010.

[23] H. Aminipour, M. Janghorban, and O. Civalek, Analysis of functionally graded doubly-curved shells with different materials via higher order shear deformation theory, Compos. Struct., vol. 251, pp. 112645, 2020. DOI: 10.1016/j.compstruct.2020.112645.

[24] A.S. Sayyad, and Y.M. Ghugal, Static and free vibration analysis of doubly-curved functionally graded material shells, Compos. Struct., vol. 269, pp. 114045, 2021. DOI: 10.1016/j.compstruct.2021.114045.

[25] A. Rachid, D. Ouinas, A. Lousdad, F.Z. Zaoui, B. Achour, H. Gasmi, T.A. Butt, and A. Tounsi, Mechanical behavior and free vibration analysis of FG doubly curved shells on elastic foundation via a new modified displacements field model of 2D and quasi-3D HSDTs, Thin-Walled Struct., vol. 172, pp. 108783, 2022. DOI: 10.1016/j.tws.2021.108783.

[26] B. Karami, D. Shahsavari, and M. Janghorban, On the dynamics of porous doubly-curved nanoshells, Int. J. Eng. Sci., vol. 143, pp. 39–55, 2019. DOI: 10.1016/j.ijengsci.2019.06.014.

[27] H. Ahmadi, A. Bayat, and N.D. Duc, Nonlinear forced vibrations analysis of imperfect stiffened FG doubly curved shallow shell in thermal environment using multiple scales method, Compos. Struct., vol. 256, pp. 113090, 2021. DOI: 10.1016/j.compstruct.2020.113090.

[28] Y. Xue, G. Jin, C. Zhang, X. Han, and J. Chen, Free vibration analysis of functionally graded porous cylindrical panels and shells with porosity distributions along the thickness and length directions, Thin-Walled Struct., vol. 184, pp. 110448, 2023. DOI: 10.1016/j.tws.2022.110448.

[29] P.H. Cong, and N.D. Duc, Nonlinear dynamic analysis of porous eccentrically stiffened double curved shallow auxetic shells in thermal environments, Thin-Walled Struct., vol. 163, pp. 107748, 2021. DOI: 10.1016/j.tws.2021.107748.

[30] A.R. Setoodeh, M. Shojaee, and P. Malekzadeh, Vibrational behavior of doubly curved smart sandwich shells with FG-CNTRC face sheets and FG porous core, Compos. Part B Eng., vol. 165, pp. 798–822, 2019. DOI: 10.1016/j.compositesb.2019.01.022.

[31] M. Karimiasl, F. Ebrahimi, and V. Mahesh, Nonlinear forced vibration of smart multiscale sandwich composite doubly curved porous shell, Thin-Walled Struct., vol. 143, pp. 106152, 2019. DOI: 10.1016/j.tws.2019.04.044.

[32] V.Q. Duong, N.D. Tran, D.T. Luat, and D. Van Thom, Static analysis and boundary effect of FG-CNTRC cylindrical shells with various boundary conditions using quasi-3D shear and normal deformations theory, Structures., vol. 44, pp. 828–850, 2022. DOI: 10.1016/j.istruc.2022.08.039.

[33] S.W. Yang, Y.X. Hao, W. Zhang, L. Yang, and L.T. Liu, Free vibration and buckling of eccentric rotating FG-GPLRC cylindrical shell using first-order shear deformation theory, Compos. Struct., vol. 263, pp. 113728, 2021. DOI: 10.1016/j.compstruct.2021.113728.

[34] H. Ma, P. Jiao, H. Li, Z. Cheng, and Z. Chen, Buckling analyses of thin-walled cylindrical shells subjected to multi-region localized axial compression: experimental and numerical study, Thin-Walled Struct., vol. 183, pp. 110330, 2023. DOI: 10.1016/j.tws.2022.110330.

[35] Y. Gui, and R. Wu, Buckling analysis of embedded thermo-magneto-electro-elastic nano cylindrical shell subjected to axial load with nonlocal strain gradient theory, Mech. Res. Commun., vol. 128, pp. 104043, 2023. DOI: 10.1016/j.mechrescom.2023.104043.

[36] T.Q. Quan, N.H. Cuong, and N.D. Duc, Nonlinear buckling and post-buckling of eccentrically oblique stiffened sandwich functionally graded double curved shallow shells, Aerosp. Sci. Technol., vol. 90, pp. 169–180, 2019. DOI: 10.1016/j.ast.2019.04.037.

[37] R. Jahangiri, M. Rezaee, and H. Manafi, Nonlinear and chaotic vibrations of FG double curved sandwich shallow shells resting on visco-elastic nonlinear Hetenyi foundation under combined resonances, Compos. Struct., vol. 295, pp. 115721, 2022. DOI: 10.1016/j.compstruct.2022.115721.

[38] Z. Jing, X. Li, Q. Sun, K. Liang, Y. Zhang, and L. Duan, A 2D-sampling optimization method for buckling layup design of doubly-curved laminated composite shallow shells, Compos. Struct., vol. 297, pp. 115934, 2022. DOI: 10.1016/j.compstruct.2022.115934.

[39] V.R. Kar, and S.K. Panda, Post-buckling behaviour of shear deformable functionally graded curved shell panel under edge compression, Int. J. Mech. Sci., vol. 115-116, pp. 318–324, 2016. DOI: 10.1016/j.ijmecsci.2016.07.014.

[40] H. Ma, W. Sun, D. Du, X. Liu, and H. Liu, Nonlinear vibration analysis of double cylindrical shells coupled structure with bolted connection and partially attached constrained layer damping, Int. J. Mech. Sci., vol. 223, pp. 107270, 2022. DOI: 10.1016/j.ijmecsci.2022.107270.

[41] Z. Hu, C. Zhou, X. Zheng, Z. Ni, and R. Li, Free vibration of non-Lévy-type functionally graded doubly curved shallow shells: new analytic solutions, Compos. Struct., vol. 304, pp. 116389, 2023. DOI: 10.1016/j.compstruct.2022.116389.

[42] B. Badarloo, S. Tayebikhorami, S.M. Mirfatah, H. Salehipour, and O. Civalek, Nonlinear forced vibration analysis of laminated composite doubly-curved shells enriched by nanocomposites incorporating foundation and thermal effects, Aerosp. Sci. Technol., vol. 127, pp. 107717, 2022. DOI: 10.1016/j.ast.2022.107717.

[43] E. Taati, F. Fallah, and M.T. Ahmadian, Subsonic and supersonic flow-induced vibration of sandwich cylindrical shells with FG-CNT reinforced composite face sheets and metal foam core, Int. J. Mech. Sci., vol. 215, pp. 106918, 2022. DOI: 10.1016/j.ijmecsci.2021.106918.

[44] X. Sun, R. Gao, and Y. Zhang, Spectral stochastic isogeometric analysis of bending and free vibration of porous functionally graded plates, Appl. Math. Model., vol. 116, pp. 711–734, 2023. DOI: 10.1016/j.apm.2022.12.017.

[45] R. Moradi-Dastjerdi, and K. Behdinan, Free vibration response of smart sandwich plates with porous CNT-reinforced and piezoelectric layers, Appl. Math. Model., vol. 96, pp. 66–79, 2021. DOI: 10.1016/j.apm.2021.03.013.

[46] Y. Wang, H. Liu, W. Zhang, and Y. Liu, A size-dependent shear deformable computational framework for transient response of GNP-reinforced metal foam cylindrical shells subjected to localized impulsive loads, Appl. Math. Model., vol. 109, pp. 578–598, 2022. DOI: 10.1016/j.apm.2022.05.018.

[47] X. Xu, E. Carrera, H. Yang, E. Daneshkhah, and R. Augello, Evaluation of stiffeners effects on buckling and post-buckling of laminated panels, Aerosp. Sci. Technol., vol. 123, pp. 107431, 2022. DOI: 10.1016/j.ast.2022.107431.

[48] E. Carrera, and D. Scano, Finite elements based on Jacobi shape functions for the free vibration analysis of beams, plates, and shells, Mech. Adv. Mater. Struct., pp. 1–9, 2023. DOI: 10.1080/15376494.2023.2219438.

[49] M. Haboussi, A. Sankar, and M. Ganapathi, Nonlinear axisymmetric dynamic buckling of functionally graded graphene reinforced porous nanocomposite spherical caps, Mech. Adv. Mater. Struct., vol. 28, no. 2, pp. 127–140, 2021. DOI: 10.1080/15376494.2018.1549296.

[50] E. Arshid, M.J. Momeni Nia, M.A. Ghorbani, Ö. Civalek, and A. Kumar, On the poroelastic vibrations of lightweight FGSP doubly-curved shells integrated with GNPs-reinforced composite coatings in thermal atmospheres, Appl. Math. Model., vol. 124, pp. 122–141, 2023. DOI: 10.1016/j.apm.2023.07.036.

[51] L.L. Ren, W. Zhang, and Y.F. Zhang, Dynamic Snap-Through and nonlinear vibrations of bistable asymmetric Cross-Ply composite laminated cantilever shell under external excitation, Mech. Syst. Signal Process., vol. 195, pp. 110193, 2023. DOI: 10.1016/j.ymssp.2023.110193.

[52] M.A. Biot, Theory of buckling of a porous slab and its thermoelastic analogy, J. Appl. Mech. Trans. ASME., vol. 31, no. 2, pp. 194–198, 1964. DOI: 10.1115/1.3629586.

[53] M. Arefi, and A.M. Zenkour, Nonlocal electro-thermo-mechanical analysis of a sandwich nanoplate containing a Kelvin–Voigt viscoelastic nanoplate and two piezoelectric layers, Acta Mech., vol. 228, no. 2, pp. 475–493, 2017. DOI: 10.1007/s00707-016-1716-0.

[54] A.G. Chanda, and D. Punera, Porosity-dependent free vibration and transient responses of functionally graded composite plates employing higher order thickness stretching model, Mech. Adv. Mater. Struct., pp. 1–26, 2022. DOI: 10.1080/15376494.2022.2138652.

[55] E. Arshid, S. Amir, and A. Loghman, On the vibrations of FG GNPs-RPN annular plates with piezoelectric/metallic coatings on Kerr elastic substrate considering size dependency and surface stress effects, Acta Mech., vol. 234, no. 9, pp. 4035–4076, 2023. DOI: 10.1007/s00707-023-03593-4.

[56] E. Arshid, S. Amir, and A. Loghman, Thermoelastic vibration characteristics of asymmetric annular porous reinforced with nano-fillers microplates embedded in an elastic medium: CNTs Vs. GNPs, Archiv.Civ.Mech.Eng., vol. 23, no. 2, pp. 100, 2023. DOI: 10.1007/s43452-023-00624-8.

[57] W. Zhang, C. Wang, and Y. Wang, Thermo-mechanical analysis of porous functionally graded graphene reinforced cylindrical panels using an improved third order shear deformable model, Appl. Math. Model., vol. 118, pp. 453–473, 2023. DOI: 10.1016/j.apm.2023.01.026.

[58] E. Arshid, S. Amir, and A. Loghman, Static and dynamic analyses of FG-GNPs reinforced porous nanocomposite annular micro-plates based on MSGT, Int. J. Mech. Sci., vol. 180, no. March, pp. 105656, 2020. DOI: 10.1016/j.ijmecsci.2020.105656.

[59] S. Amir, E. Arshid, and M.R. Ghorbanpour Arani, Size-dependent magneto-electro-elastic vibration analysis of FG saturated porous annular/circular micro sandwich plates embedded with nano-composite face sheets subjected to multi-physical pre loads, Smart Struct. Syst., vol. 23, no. 5, pp. 429–447, 2019. DOI: 10.12989/sss.2019.23.5.429.

[60] D. Shahsavari, B. Karami, H.R. Fahham, and L. Li, On the shear buckling of porous nanoplates using a new size-dependent quasi-3D shear deformation theory, Acta Mech., vol. 229, no. 11, pp. 4549–4573, 2018. DOI: 10.1007/s00707-018-2247-7.

[61] Q. Li, D. Wu, X. Chen, L. Liu, Y. Yu, and W. Gao, Nonlinear vibration and dynamic buckling analyses of sandwich functionally graded porous plate with graphene platelet reinforcement resting on Winkler–Pasternak elastic foundation, Int. J. Mech. Sci., vol. 148, pp. 596–610, 2018. DOI: 10.1016/j.ijmecsci.2018.09.020.

[62] M.C. Kiran, Thermal and hygrothermal buckling characteristics of porous magneto-electro-elastic skewed plates using third-order shear deformation theory, Mech. Adv. Mater. Struct., pp. 1–16, 2023. DOI: 10.1080/15376494.2023.2227185.

[63] R. Zhong, B. Qin, Q. Wang, W. Shao, and C. Shuai, Prediction of the in-plane vibration behavior of porous annular plate with porosity distributions in the thickness and radial directions, Mech. Adv. Mater. Struct., vol. 29, no. 25, pp. 4206–4223, 2022. DOI: 10.1080/15376494.2021.1922960.

[64] E. Arshid, and S. Amir, Size-dependent vibration analysis of fluid-infiltrated porous curved microbeams integrated with reinforced functionally graded graphene platelets face sheets considering thickness stretching effect, Proc. Inst. Mech. Eng. Part L J. Mater. Des. Appl., vol. 235, no. 5, pp. 1077–1099, 2021. DOI: 10.1177/1464420720985556.

[65] R.D. Mindlin, Influence of rotatory inertia and shear on flexural motions of isotropic, elastic plates, J. appl. Mech., vol. 18, no. 1, pp. 31–38, 1951. DOI: 10.1115/1.4010217.

[66] E.M.R. Bidgoli, M. Arefi, and M. Mohammadimehr, Free vibration analysis of honeycomb doubly curved shell integrated with CNT-reinforced piezoelectric layers, Mech. Based Des. Struct.

Mach., vol. 50, no. 12, pp. 4409–4440, 2022. DOI: 10.1080/15397734.2020.1836969.

[67] Y. Yan, B. Liu, Y. Xing, E. Carrera, and A. Pagani, Free vibration analysis of variable stiffness composite laminated beams and plates by novel hierarchical differential quadrature finite elements, Compos. Struct., vol. 274, pp. 114364, 2021. DOI: 10.1016/j.compstruct.2021.114364.

[68] V. Jain, and R. Kumar, Geometrically nonlinear dynamic analysis of a damped porous microplate resting on elastic foundations under transverse patch loadings, Mech. Adv. Mater. Struct., pp. 1–24, 2023. DOI: 10.1080/15376494.2023.2216273.

[69] K. Foroutan, E. Carrera, and H. Ahmadi, Nonlinear hygrothermal vibration and buckling analysis of imperfect FG-CNTRC cylindrical panels embedded in viscoelastic foundations, Eur. J. Mech. A/Solids., vol. 85, pp. 104107, 2021. DOI: 10.1016/j.euromechsol.2020.104107.

[70] L. Zhou, A novel similitude method for predicting natural frequency of FG porous plates under thermal environment, Mech. Adv. Mater. Struct., vol. 29, no. 27, pp. 6786–6802, 2022. DOI: 10.1080/15376494.2021.1985197.

[71] M. Afzali, M. Farrokh, and E. Carrera, Thermal buckling loads of rectangular FG plates with temperature-dependent properties using Carrera Unified Formulation, Compos. Struct., vol. 295, pp. 115787, 2022. DOI: 10.1016/j.compstruct.2022.115787.

[72] P.M. Vuong, and N.D. Duc, Nonlinear buckling and post-buckling behavior of shear deformable sandwich toroidal shell segments with functionally graded core subjected to axial compression and thermal loads, Aerosp. Sci. Technol., vol. 106, pp. 106084, 2020. DOI: 10.1016/j.ast.2020.106084.

[73] M. Mohammadimehr, E. Arshid, S.M.A.R. Alhosseini, S. Amir, and M.R.G. Arani, Free vibration analysis of thick cylindrical MEE composite shells reinforced CNTs with temperature-dependent properties resting on viscoelastic foundation, Struct. Eng. Mech., vol. 70, no. 6, pp. 683–702, 2019. DOI: 10.12989/sem.2019.70.6.683.

[74] P. Tan, N. Nguyen-Thanh, T. Rabczuk, and K. Zhou, Static, dynamic and buckling analyses of 3D FGM plates and shells via an isogeometric-meshfree coupling approach, Compos. Struct., vol. 198, pp. 35–50, 2018. DOI: 10.1016/j.compstruct.2018.05.012.

[75] D.T. Huan, T.M. Tu, and T.H. Quoc, Analytical solutions for bending, buckling and vibration analysis of functionally graded cylindrical panel, JST., vol. 55, no. 5, pp. 587, 2017. DOI: 10.15625/2525-2518/55/5/8843.

[76] T. Cuong-Le, K.D. Nguyen, N. Nguyen-Trong, S. Khatir, H. Nguyen-Xuan, and M. Abdel-Wahab, A three-dimensional solution for free vibration and buckling of annular plate, conical, cylinder and cylindrical shell of FG porous-cellular materials using IGA, Compos. Struct., vol. 259, pp. 113216, 2021. DOI: 10.1016/j.compstruct.2020.113216.

[77] X. Zhao, and K.M. Liew, A mesh-free method for analysis of the thermal and mechanical buckling of functionally graded cylindrical shell panels, Comput Mech., vol. 45, no. 4, pp. 297–310, 2010. DOI: 10.1007/s00466-009-0446-8.

[78] M. Javani, Y. Kiani, and M.R. Eslami, Thermal buckling of FG graphene platelet reinforced composite annular sector plates, Thin-Walled Struct., vol. 148, pp. 106589, 2020. DOI: 10.1016/j.tws.2019.106589.

[79] M. Jabbari, M. Hashemitaheri, A. Mojahedin, and M.R. Eslami, Thermal buckling analysis of functionally graded thin circular plate made of saturated porous materials, J. Therm. Stress., vol. 37, no. 2, pp. 202–220, 2014. DOI: 10.1080/01495739.2013.839768.

[80] E. Arshid, S. Amir, and A. Loghman, Thermal buckling analysis of FG graphene nanoplatelets reinforced porous nanocomposite MCST-based annular/circular microplates, Aerosp. Sci. Technol., vol. 111, pp. 106561, 2021. DOI: 10.1016/j.ast.2021.106561.

[81] H. Wu, S. Kitipornchai, and J. Yang, Thermal buckling and postbuckling of functionally graded graphene nanocomposite plates, Mater. Des., vol. 132, pp. 430–441, 2017. DOI: 10.1016/j.matdes.2017.07.025.

Appendix: The stiffness matrix arrays used in Eq. (46) are defined as below:

$$K_{11} = \eta_1\ \mathrm{A}^2 - \frac{\kappa_s\ \eta_{13}}{R_{\varsigma_1}{}^2} + \eta_{15}\ \mathrm{B}^2 + \frac{\eta_{16}\ \mathrm{B}^2}{R_{\varsigma_1}} + \left(\frac{R_{\varsigma_2} - R_{\varsigma_1}}{2R_{\varsigma_1}R_{\varsigma_2}}\right)\eta_{16}\ \mathrm{B}^2 + \left(\frac{R_{\varsigma_2} - R_{\varsigma_1}}{2R_{\varsigma_1}R_{\varsigma_2}}\right)\frac{\eta_{17}\ \mathrm{B}^2}{R_{\varsigma_1}}, \tag{A-1}$$

$$K_{12} = \eta_4\ \mathrm{AB} + \eta_{15}\ \mathrm{AB} + \frac{\eta_{16}\ \mathrm{A}\ \mathrm{B}}{R_{\varsigma_2}} + \left(\frac{R_{\varsigma_2} - R_{\varsigma_1}}{2R_{\varsigma_1}R_{\varsigma_2}}\right)\eta_{16}\ \mathrm{AB} + \left(\frac{R_{\varsigma_2} - R_{\varsigma_1}}{2R_{\varsigma_1}R_{\varsigma_2}}\right)\frac{\eta_{17}\ \mathrm{AB}}{R_{\varsigma_2}},$$

$$K_{13} = -\frac{\eta_1\mathrm{A}}{R_{\varsigma_1}} - \frac{\eta_4\mathrm{A}}{R_{\varsigma_2}} - \frac{\kappa_s\ \eta_{13}\mathrm{A}}{R_{\varsigma_1}},$$

$$K_{14} = \eta_2\ \mathrm{A}^2 - \frac{\kappa_s\eta_{13}}{R_{\varsigma_1}} + \eta_{16}\ \mathrm{B}^2 + \left(\frac{R_{\varsigma_2} - R_{\varsigma_1}}{2R_{\varsigma_1}R_{\varsigma_2}}\right)\eta_{17}\ \mathrm{B}^2,$$

$$K_{15} = \left(\frac{R_{\varsigma_2} - R_{\varsigma_1}}{2R_{\varsigma_1}R_{\varsigma_2}}\right)\eta_{17}\ \mathrm{AB} + \eta_{16}\ \mathrm{AB} + \eta_5\ \mathrm{AB},$$

$$K_{21} = \eta_7\ \mathrm{AB} + \eta_{15}\ \mathrm{AB} + \frac{\eta_{16}\ \mathrm{AB}}{R_{\varsigma_1}} - \left(\frac{R_{\varsigma_2} - R_{\varsigma_1}}{2R_{\varsigma_1}R_{\varsigma_2}}\right)\eta_{16}\ \mathrm{AB} - \left(\frac{R_{\varsigma_2} - R_{\varsigma_1}}{2R_{\varsigma_1}R_{\varsigma_2}}\right)\frac{\eta_{17}\ \mathrm{AB}}{R_{\varsigma_1}},$$

$$K_{22} = \eta_{10}\ \mathrm{B}^2 - \frac{\kappa_s\ \eta_{14}}{R_{\varsigma_2}{}^2} + \eta_{15}\ \mathrm{A}^2 + \frac{\eta_{16}\ \mathrm{A}^2}{R_{\varsigma_2}} - \left(\frac{R_{\varsigma_2} - R_{\varsigma_1}}{2R_{\varsigma_1}R_{\varsigma_2}}\right)\eta_{16}\ \mathrm{A}^2 - \left(\frac{R_{\varsigma_2} - R_{\varsigma_1}}{2R_{\varsigma_1}R_{\varsigma_2}}\right)\frac{\eta_{17}\ \mathrm{A}^2}{R_{\varsigma_2}},$$

$$K_{23} = -\frac{\eta_7\mathrm{B}}{R_{\varsigma_1}} - \frac{\eta_{10}\mathrm{B}}{R_{\varsigma_2}} - \frac{\kappa_s\ \eta_{14}\mathrm{B}}{R_{\varsigma_2}},$$

$$K_{24} = -\left(\frac{R_{\varsigma_2} - R_{\varsigma_1}}{2R_{\varsigma_1}R_{\varsigma_2}}\right)\eta_{17}\ \mathrm{AB} + \eta_{16}\ \mathrm{AB} + \eta_8\ \mathrm{AB},$$

$$K_{25} = \eta_{11}\ \mathrm{B}^2 - \frac{\kappa_s\ \eta_{14}}{R_{\varsigma_2}} + \eta_{16}\ \mathrm{A}^2 - \left(\frac{R_{\varsigma_2} - R_{\varsigma_1}}{2R_{\varsigma_1}R_{\varsigma_2}}\right)\eta_{17}\ \mathrm{A}^2,$$

$$K_{31} = -\frac{\eta_1\mathrm{A}}{R_{\varsigma_1}} - \frac{\eta_7\mathrm{A}}{R_{\varsigma_2}} + \frac{\kappa_s\ \eta_{13}\mathrm{A}}{R_{\varsigma_1}},$$

$$K_{32} = -\frac{\eta_4\mathrm{B}}{R_{\varsigma_1}} - \frac{\eta_{10}\mathrm{B}}{R_{\varsigma_2}} + \frac{\kappa_s\ \eta_{14}\mathrm{B}}{R_{\varsigma_2}},$$

$$K_{33} = \frac{\eta_1}{R_{\varsigma_1}{}^2} + \frac{\eta_4}{R_{\varsigma_1}\ R_{\varsigma_2}} + \frac{\eta_7}{R_{\varsigma_1}\ R_{\varsigma_2}} + \frac{\eta_{10}}{R_{\varsigma_2}{}^2} + \kappa_s\ \eta_{13}\ \mathrm{A}^2 + \kappa_s\eta_{14}\ \mathrm{B}^2 - K_W - K_P\ \mathrm{A}^2 - K_P\ \mathrm{B}^2 - N^T_{\varsigma_1}\mathrm{A}^2 - N^T_{\varsigma_2}\mathrm{B}^2 - N^M_{\varsigma_1}\mathrm{A}^2 - N^M_{\varsigma_2}\mathrm{B}^2,$$

$$K_{34} = -\frac{\eta_2\mathrm{A}}{R_{\varsigma_1}} - \frac{\eta_8\mathrm{A}}{R_{\varsigma_2}} + \kappa_s\ \eta_{13}\mathrm{A},$$

$$K_{35} = -\frac{\eta_5 \mathrm{B}}{R_{\varsigma_1}} - \frac{\eta_{11} \mathrm{B}}{R_{\varsigma_2}} + \kappa_s \eta_{14} \mathrm{B},$$

$$K_{41} = \eta_2 \mathrm{A}^2 + \frac{\kappa_s \eta_{13}}{R_{\varsigma_1}} + \eta_{16}\ \mathrm{B}^2 + \frac{\eta_{17} \mathrm{B}^2}{R_{\varsigma_1}},$$

$$K_{42} = \eta_5\ \mathrm{AB} + \eta_{16}\ \mathrm{AB} + \frac{\eta_{17}\ \mathrm{AB}}{R_{\varsigma_2}},$$

$$K_{43} = -\frac{\eta_2 \mathrm{A}}{R_{\varsigma_1}} - \frac{\eta_5 \mathrm{A}}{R_{\varsigma_2}} + \kappa_s\ \eta_{13} \mathrm{A},$$

$$K_{44} = \eta_{17} \mathrm{B}^2 + \eta_3 \mathrm{A}^2 + \kappa_s \eta_{13},$$

$$K_{45} = \eta_{17}\ \mathrm{AB} + \eta_6\ \mathrm{AB},$$

$$K_{51} = \eta_8 \mathrm{AB} + \eta_{16}\ \mathrm{AB} + \frac{\eta_{17}\ \mathrm{AB}}{R_{\varsigma_1}},$$

$$K_{52} = \eta_{11}\ \mathrm{B}^2 + \frac{\kappa_s\ \eta_{14}}{R_{\varsigma_2}} + \eta_{16}\ \mathrm{A}^2 + \frac{\eta_{17}\ \mathrm{A}^2}{R_{\varsigma_2}},$$

$$K_{53} = -\frac{\eta_8 \mathrm{B}}{R_{\varsigma_1}} - \frac{\eta_{11} \mathrm{B}}{R_{\varsigma_2}} + \kappa_s\ \eta_{14} \mathrm{B},$$

$$K_{54} = \eta_{17}\ \mathrm{AB} + \eta_9\ \mathrm{AB},$$

$$K_{55} = \eta_{12}\ \mathrm{B}^2 + \eta_{17}\ \mathrm{A}^2 + \eta_{14}\ \kappa_s$$

The hired integral coefficients in the above arrays are defined as follows:

$$\begin{aligned}
&\begin{Bmatrix} \eta_1 \\ \eta_2 \\ \eta_3 \end{Bmatrix} = \int_z Q_{11}^{c,f}(z) \begin{Bmatrix} 1 \\ z \\ z^2 \end{Bmatrix} \mathrm{d}z, \quad \begin{Bmatrix} \eta_4 \\ \eta_5 \\ \eta_6 \end{Bmatrix} = \int_z Q_{12}^{c,f}(z) \begin{Bmatrix} 1 \\ z \\ z^2 \end{Bmatrix} \mathrm{d}z, \\
&\begin{Bmatrix} \eta_7 \\ \eta_8 \\ \eta_9 \end{Bmatrix} = \int_z Q_{21}^{c,f}(z) \begin{Bmatrix} 1 \\ z \\ z^2 \end{Bmatrix} \mathrm{d}z, \quad \begin{Bmatrix} \eta_{10} \\ \eta_{11} \\ \eta_{12} \end{Bmatrix} = \int_z Q_{22}^{c,f}(z) \begin{Bmatrix} 1 \\ z \\ z^2 \end{Bmatrix} \mathrm{d}z, \\
&\begin{Bmatrix} \eta_{13} \\ \eta_{14} \end{Bmatrix} = \int_z \begin{Bmatrix} Q_{55}^{c,f}(z) \\ Q_{44}^{c,f}(z) \end{Bmatrix} \mathrm{d}z, \quad \begin{Bmatrix} \eta_{15} \\ \eta_{16} \\ \eta_{17} \end{Bmatrix} = \int_z Q_{66}^{c,f}(z) \begin{Bmatrix} 1 \\ z \\ z^2 \end{Bmatrix} \mathrm{d}z
\end{aligned} \tag{A-2}$$